



HAL
open science

Arctic mixed-phase clouds simulated by the WRF model: Comparisons with ACLOUD radar and in situ airborne observations and sensitivity of microphysics properties

Diana Arteaga, Céline Planche, Frédéric Tridon, Régis Dupuy, Antoine Baudoux, Sandra Banson, Jean-Luc Baray, Guillaume Mioche, André Ehrlich, Mario Mech, et al.

► To cite this version:

Diana Arteaga, Céline Planche, Frédéric Tridon, Régis Dupuy, Antoine Baudoux, et al.. Arctic mixed-phase clouds simulated by the WRF model: Comparisons with ACLOUD radar and in situ airborne observations and sensitivity of microphysics properties. Atmospheric Research, In press, 10.1016/j.atmosres.2024.107471 . hal-04574295

HAL Id: hal-04574295

<https://hal.science/hal-04574295>

Submitted on 14 May 2024

HAL is a multi-disciplinary open access archive for the deposit and dissemination of scientific research documents, whether they are published or not. The documents may come from teaching and research institutions in France or abroad, or from public or private research centers.

L'archive ouverte pluridisciplinaire **HAL**, est destinée au dépôt et à la diffusion de documents scientifiques de niveau recherche, publiés ou non, émanant des établissements d'enseignement et de recherche français ou étrangers, des laboratoires publics ou privés.



Distributed under a Creative Commons Attribution - NonCommercial 4.0 International License

1 Arctic mixed-phase clouds simulated by the WRF model: 2 Comparisons with ALOUD radar and *in situ* airborne observations 3 and sensitivity of microphysics properties

4 Diana Arteaga⁽¹⁾, Céline Planche^(1,2,*), Frédéric Tridon^(3,1), Régis Dupuy⁽¹⁾, Antoine Baudoux⁽¹⁾,
5 Sandra Banson⁽¹⁾, Jean-Luc Baray⁽¹⁾, Guillaume Mioche⁽¹⁾, André Ehrlich⁽⁴⁾, Mario Mech⁽⁵⁾,
6 Stephan Mertes⁽⁶⁾, Manfred Wendisch⁽⁴⁾, Wolfram Wobrock⁽¹⁾ and Olivier Jourdan^(1,*)

7 ⁽¹⁾ Université Clermont Auvergne (UCA), CNRS-INSU, Laboratoire de Météorologie Physique (LaMP), OPGC, F-
8 63000 Clermont-Ferrand, France.

9 ⁽²⁾ Institut Universitaire de France (IUF).

10 ⁽³⁾ DIATI, Politecnico di Torino, Turin, Italy.

11 ⁽⁴⁾ Universität Leipzig, Leipziger Institut für Meteorologie, Stephanstr. 3, 04103 Leipzig, Germany.

12 ⁽⁵⁾ University of Cologne, Institute for Geophysics and Meteorology, Cologne, Germany.

13 ⁽⁶⁾ Leibniz Institute for Tropospheric Research (TROPOS), Atmospheric Microphysics Department, Permoserstraße
14 15, D-04318 Leipzig, Germany

15 Corresponding authors^(*): celine.planche@uca.fr & olivier.jourdan@uca.fr

16

17 Highlights

- 18 ● Mixed-phase cloud microphysical properties vary with the underlying surface
- 19 ● Cloud representation improves with finer vertical resolution for initialisation data
- 20 ● The boundary layer and microphysical schemes impact the cloud vertical properties
- 21 ● The ice crystal number and mass concentrations are underestimated by the model
- 22 ● Both ice and liquid water contents increase with droplet number concentration

23 Abstract

24 The microphysical properties of two mixed-phase clouds (MPCs), one over sea ice, and
25 another over open ocean, are investigated using *in situ* measuring probes and a cloud radar
26 installed on-board two aircraft during the Arctic CLOUD Observations Using Airborne
27 measurements during polar Day (ALOUD) field campaign, west of Svalbard on 17 June 2017.
28 Comparisons between observations and different configurations of the Weather and Research
29 Forecasting (WRF) model are conducted and reveal discrepancies in the vertical profile of the
30 ice crystal concentrations for both MPCs due to slightly higher temperatures (by approx. 1-
31 2°C) in WRF than observed, affecting the ice formation. A comprehensive sensitivity analysis
32 is carried out to address the impact of assumptions used for the microphysics (MP) and the
33 atmospheric boundary layer (ABL) schemes on the simulated vertical properties of the MPC
34 systems. The role of the vertical resolution of the large scale data used for model initialisation
35 is also investigated. Results show that the model performance improves for large-scale
36 initialisation with more numerous levels close to the surface. Moreover, modifying the ABL or
37 MP scheme influences the altitudes of the cloud top and base as well as the liquid and ice
38 water amounts. Our study also highlights how an increase in the cloud condensation nuclei
39 and droplet number concentrations can impact the vertical profiles of the liquid and ice water
40 amounts.

41 **Keywords:** Arctic cloud microphysical properties, WRF modelling, cloud condensation nuclei,
42 surface properties.

1

2 1. Introduction

3 Mixed-phase clouds (MPCs) are frequently occurring in the Arctic: they can persist over several
4 days under different meteorological conditions (e.g., Shupe and Intrieri, 2004; Morrison et al.,
5 2012; Mioche et al., 2015). These clouds are generally composed of one or several distinct
6 stratiform layers consisting of supercooled water droplets embedded near the top of an ice
7 cloud (Curry et al., 2000; Korolev et al., 2003; Shupe et al., 2011). Single-layer stratocumulus
8 MPCs have been extensively studied in the western and European Arctic (Shupe et al., 2006;
9 Gayet et al., 2009; McFarquhar et al., 2011; Morrison et al., 2012; Lloyd et al., 2015; Mioche
10 et al., 2017; Achtert et al., 2020; Järvinen et al., 2023). These atmospheric boundary layer
11 (ABL) clouds are sustained by weak updrafts and may cover wide areas in the Arctic. The
12 MPCs peculiar microphysical properties associated with their high frequency of occurrence
13 contribute to the strong impact on the energy budget and the hydrological cycle exerted by
14 these clouds in the ABL (de Boer et al., 2011; Kay et al., 2012; Matus and l'Ecuyer, 2017;
15 McIlhatten et al., 2020; Wendisch et al., 2023a). Despite the significant advances achieved on
16 the basis of active remote sensing observations, estimates of the radiative effect and the
17 precipitation frequency of low-level MPCs are still uncertain.

18 Complex interactions between local microphysical, radiative, dynamical processes and larger
19 scale environmental conditions regulate the life cycle of MPCs (Klein et al., 2009; Solomon et
20 al., 2011; Morrison et al., 2012). Major field experiments involving airborne measurements
21 combined with modelling studies have given an insight of the main microphysical processes
22 and properties within low-level MPCs. These clouds are typically 500 to 3000 m thick and are
23 often observed at temperatures between -30°C and -2°C (Shupe et al., 2006; McFarquhar et
24 al., 2007; Gayet et al., 2009). Within low-level Arctic MPCs, the liquid water content (LWC)
25 increases almost linearly with altitude as supercooled droplets grow by condensation of water
26 vapour due to the cooling in the ascending air parcels (Jackson et al., 2012; Mioche et al.,
27 2017; Achtert et al., 2020). At cloud top, temperature inversions and the associated
28 entrainment of dry air lead to the evaporation of a fraction of liquid water droplets (Klingebiel
29 et al., 2015; de Lozar and Muessle, 2016), limiting the vertical development of MPCs. Humidity
30 inversions may occur at the cloud top, supplying moisture to the upper cloud layers by
31 entrainment (Nygard et al., 2014; Pithan et al., 2016; Egerer et al., 2021). This may prevent
32 evaporation of liquid water droplets and contribute to the persistence of the MPCs (Solomon
33 et al., 2011; de Lozar and Muessle, 2016). However, cloud top radiative cooling seems to be
34 the dominant local mechanism responsible for the maintenance of the liquid water phase. The
35 cloud top cooling generates downdrafts causing instabilities in the lower cloud layers, triggering
36 further turbulent updrafts that promote the growth of water droplets (Harrington et al., 1999;
37 Morrison et al., 2012; Wendisch et al., 2019).

38 The cloud processes responsible for the production of ice crystals in the upper part of the cloud
39 seem to be driven by the cloud top temperature, as well as turbulent processes and
40 entrainment at cloud top (Savre and Ekman, 2015a, 2015b; Chylik et al., 2023). However, the
41 representation of these processes in models and their quantification remain highly uncertain.
42 Accurate *in situ* measurements of small ice crystals with sizes typically less than $50\ \mu\text{m}$ are
43 sparse and are also subject to high uncertainties (Jourdan et al., 2010; Wendisch and
44 Brenguier, 2013). The assessment of ice nucleating-particles (INP) number concentrations that
45 trigger the initiation of ice crystals and their temporal evolution is crucial but also relies on a
46 limited set of *in situ* observations (Irish et al., 2019; Wex et al., 2019; Hartmann et al., 2022).
47 Although heterogeneous nucleation seems to be the main mechanism for ice crystal formation,
48 there is no consensus on the predominant nucleation mode occurring in low-level MPCs (de

1 Boer et al., 2010; Solomon et al., 2015; Fan et al., 2016). Large eddy simulations tend to point
2 out that immersion freezing or contact freezing are the most active nucleation modes in MPC
3 characterised by moderate liquid water path and high ice crystal number concentrations
4 (Fridlind et al., 2012; Young et al., 2017) or persistent MPCs (Fridlind and Ackerman, 2018).
5 These studies also show that the thermodynamic structure of the lower troposphere and the
6 heat and humidity fluxes in the ABL influence the ice crystal nucleation. Since most of the
7 modelling studies fail to reproduce the correct number of observed ice crystals (Ovchinnikov
8 et al., 2014), other ice formation processes may also occur in MPCs such as secondary ice
9 production (Field et al., 2017; Pasquier et al., 2022) or the recycling of INP through sub-cloud
10 sublimation (Solomon et al., 2015). For instance, Zhao and Liu (2020) or Karalis et al. (2022)
11 have shown that secondary ice production processes can significantly contribute to the
12 formation of ice crystals and influence the phase partitioning and the amount of precipitation.

13 Within MPCs, ice crystals strongly interact with the water droplets. They can grow by riming
14 due to the collection of droplets by ice crystals (Korolev et al., 2006; McFarquhar et al., 2007;
15 Waitz et al., 2022), leading to complex shapes (Gayet et al., 2009; Mioche et al., 2017; Järvinen
16 et al., 2023). The Wegener-Bergeron-Findeisen mechanism is also very efficient in growing
17 the ice crystals by water vapour deposition at the expense of liquid water droplets, thus, leading
18 to more pristine crystal shapes such as columns, plates or dendrites (Mioche and Jourdan,
19 2018). While the Wegener-Bergeron-Findeisen process should lead to rapid glaciation of the
20 MPC, it can be counterbalanced by updraft and turbulence induced by the cloud top radiative
21 cooling maintaining the liquid water phase. The dynamics with updrafts and downdrafts also
22 plays a crucial role by transporting the ice particles into the cloud, which promotes ice crystal
23 aggregation forming irregular shapes (Korolev et al., 1999; Solomon et al., 2011). This partly
24 explains why most of the time, the ice crystal microphysical properties do not vary significantly
25 within the MPCs, except in the lowest cloud layer where large ice crystals precipitate down to
26 the surface (Gayet et al., 2009; Lloyd et al., 2015; Mioche et al., 2017).

27 Furthermore, the life cycle and the microphysical properties of low-level MPCs are impacted
28 by environmental conditions at larger spatial and temporal scales. The synoptic situation, heat
29 and humidity advection, long-range transport of aerosol particles and surface type (e.g., open
30 ocean or sea ice) interact with local processes to modify the persistence and the phase
31 partitioning of MPCs (Boisvert et al., 2015; Young et al., 2017; Coopman et al., 2018;
32 Sotiropoulou et al., 2018; Moser et al., 2023). For instance, warm air intrusions are generally
33 associated with higher aerosol particle number concentrations and cloud condensation nuclei
34 (CCN), which result in a larger number of small liquid droplets mitigating the formation of ice
35 crystals, their growth and precipitation efficiencies (Lance et al., 2011; Jackson et al., 2012;
36 Mioche et al., 2017; Keita et al., 2020). A limited number of studies have also investigated
37 changes in cloud microphysical properties induced by the surface type with sometimes
38 contradictory results (Lloyd et al., 2015; Young et al., 2016; Eirund et al., 2019; Järvinen et al.,
39 2023; Klingebiel et al., 2023; Moser et al., 2023). During the Aerosol-Cloud Coupling And
40 Climate Interactions in the Arctic (ACCACIA) campaign, Young et al. (2016) showed that the
41 ice crystal number concentration did not vary significantly with the surface type while the
42 measured droplet number concentration was twice as high over sea ice as over open ocean,
43 which was similarly reported by Moser et al. (2023) and Klingebiel et al. (2023). First results
44 obtained during the Arctic Cloud Observations Using airborne measurements during polar Day
45 (ACLOUD) (Ehrlich et al., 2019; Wendisch et al., 2019) and the Joint Aircraft campaign
46 observing FLUXes of energy and momentum in the cloudy ABL over polar sea ice and ocean
47 (AFLUX) (Mech et al., 2022) airborne campaigns point towards a larger variability of the ice
48 phase microphysical properties with the surface conditions during cold air outbreaks (Mech et
49 al., 2022) and higher number concentrations of small droplets over the open sea during warm
50 air intrusions (Dupuy et al., 2018). However most studies argue that the thermodynamic

1 structure and dynamics of the ABL play a key role on the phase distribution within low-level
2 MPCs. For instance, larger cloud particle sizes and water contents were observed over open
3 ocean compared to cloud properties over sea ice as a result of increased heat fluxes and
4 turbulence over ice-free water (Young et al., 2016; Eirund et al., 2019; Klingebiel et al., 2023;
5 Moser et al., 2023).

6 This network of interactions between numerous fast-timescale local processes and large- scale
7 conditions complicates the interpretation of measurements and the realistic representation of
8 low-level MPC properties in weather and climate models (Klein et al., 2009; Morrison et al.,
9 2012) where the physical processes are parameterised. In particular, the modelling of the life
10 cycle of MPC is hampered by over-simplified assumptions (used in parameterisations) to
11 represent mixed-phase microphysical processes and ABL dynamics (Pithan et al., 2016;
12 Korolev et al., 2017; Fridlind and Ackerman, 2018; Tan and Storelvomo 2019). The ice crystal
13 number concentration is a critical parameter in this regard as it influences the liquid/ice
14 partitioning within the MPCs and its longevity (Ovchinnikov et al., 2014; Solomon et al., 2018).
15 An inaccurate increase of the predicted nucleated ice crystals can lead to a substantially
16 reduced liquid water path, a rapid glaciation, and a dissipation of the MPC (Prenni et al., 2007;
17 Murray et al., 2012; Young et al., 2017). Most of the cloud-resolving models apply
18 parameterisations of primary ice formation derived in the midlatitudes, which results in an
19 inadequate forecast of the ice number concentrations and the phase partitioning (Tjernström
20 et al., 2008; Morrison et al., 2009; de Boer et al., 2011). In two-moment bulk microphysical
21 models, only the total number and the mass of the ice crystal population are prognosed. Even
22 when single ice crystal properties that control ice growth and sedimentation are set identical in
23 all the models, previous intercomparison studies of single layer MPC evolutions showed
24 extremely high differences in the predicted ice crystal number concentration and the simulated
25 liquid and ice water contents (Klein et al., 2009, Stevens et al., 2018).

26 The discrepancies result from the parameterisation of the ice formation processes and the way
27 the hydrometeors particle size distributions and the droplet-ice interactions are represented
28 (Fridlind et al., 2007; Morrison et al., 2009; Avramov et al., 2011; de Boer et al., 2011;
29 Ovchinnikov et al., 2014; Young et al., 2017 ; Stevens et al., 2018).

30 In this study, the main objective is to investigate the performance of the Weather Research
31 and Forecasting (WRF) model to realistically simulate the microphysical properties of Arctic
32 low-level MPCs. Cho et al. (2020) showed that Polar WRF can reasonably reproduce the mean
33 ice water profiles, the cloud amount and top height based on comparisons with spaceborne
34 lidar-radar retrievals. They also highlighted the high sensitivity of the vertical structure of the
35 microphysical properties of wintertime low-level mixed phase clouds and the longwave
36 radiative fluxes to the choice of the microphysics scheme (i.e., the double moment scheme of
37 Morrison et al. (2009) or the single-moment scheme of Hong and Lim (2006)). In particular,
38 significant discrepancies in the simulated liquid phase properties and in the distribution of the
39 occurrence of the liquid or mixed-phase with the temperature were reported. Moreover, the
40 simulated vertical distribution of water droplet properties could not be confirmed by the
41 observations as liquid water profiles can hardly be retrieved from lidar/radar measurements.
42 Accurate simulation of the liquid phase, especially in springtime and summertime MPCs, is
43 essential since previous modelling studies have established the importance of interactions
44 between ice and liquid processes on the evolution of MPC microphysical properties (Klein et
45 al., 2009; Solomon et al., 2018). In this respect, Polar WRF simulations presented in Hines
46 and Bromwich (2017) were in better agreement with surface radiative flux observations when
47 the prescribed cloud droplet number concentrations were constrained by values representative
48 of the Arctic environment. In pristine conditions (i.e. low CCN concentrations), intercomparison
49 of large eddy simulation (LES) models and numerical weather prediction models (including

1 WRF) resulted in a wide inter-model diversity in the simulated liquid (and ice) water paths
2 which were found to be highly sensitive to changes in cloud droplet or CCN concentrations
3 (Stevens et al., 2018). However, LES experiments carried out on ACCACIA case studies
4 showed that the response of MPC microphysical and macrophysical properties to aerosol
5 perturbations seems to vary with the surface conditions which impact the turbulent fluxes, the
6 updraft velocities and the moisture of the ABL (Young et al., 2017, 2018; Eirund et al., 2019).
7 Over open ocean, increasing the concentration of CCN (from 100 to 200 cm^{-3}) immediately
8 lead to higher droplet concentration and liquid water path as well as the formation of new ice
9 crystals by immersion freezing whereas the activation of CCN was less efficient and delayed
10 in MPCs over sea ice. INP perturbations (from 3 to 10 L^{-1}) resulted in an increase of the cloud
11 ice water path and a decrease of the liquid water path regardless of the surface conditions
12 (Eirund et al., 2019). These modelling studies, associated with the work of Kretzschmar et al.
13 (2020) suggest that, in order to evaluate the representation of MPC microphysical properties,
14 physical processes (including aerosol-cloud interactions) in models, airborne observations of
15 the vertical structure of MPC and of the thermodynamics of the ABL are still needed. In
16 particular, in situ measurements of the hydrometeor size distributions, CCN concentrations
17 and radiative fluxes combined with active remote sensing observations over different surface
18 and meteorological conditions are valuable to conduct sensitivity tests and to evaluate and
19 constrain microphysical schemes.

20 In this framework, the flight plan and measurements performed during the ACLOUD campaign
21 enabled us to target two MPC systems observed over two different types of surface on 17 June
22 2017 that are used to test the modelling capabilities of WRF. Section 2 describes the vertical
23 microphysical structure of the two MPC systems, one observed over open ocean and the other
24 over sea ice using in situ and active remote sensing measurements installed on the Polar 5
25 and Polar 6 aircraft of the German Alfred Wegener Institute for Polar and Marine Research
26 (AWI) (Wesche et al., 2016; Ehrlich et al., 2019). The WRF simulations of the two MPCs are
27 presented in Section 3 with a focus on the impact of the thermodynamic structure of the ABL
28 and the microphysical parameterisations on the cloud properties. In Section 4, a sensitivity
29 study is carried out to address the influence of aerosol particle pollution (i.e., CCN number
30 concentration) on the cloud phase partitioning. Finally, Section 5 discusses the limitations of
31 the simulations and observations as well as the consequences of the microphysical
32 assumptions used in WRF, especially the choice of a prescribed size distribution.

33 **2. ACLOUD observations**

34 The ACLOUD field study was conducted within the framework of the "Arctic Amplification:
35 climate relevant atmospheric and surface processes, and feedback mechanisms" (AC)³ project
36 (Wendisch et al., 2017, 2019, 2023b). It took place in the North-West of the Svalbard
37 archipelago (covering 76-81°N and 10-28°E) between 23 May and 26 June 2017. This region
38 is known to be influenced by different air mass types (e.g., intrusions of warm air from the
39 South or cold air from the central Arctic) and by long-range transport of aerosol particles and
40 gaseous pollutants from the midlatitudes (Knudsen et al., 2018; Wendisch et al., 2023b). As
41 shown in Knudsen et al. (2018), various synoptic conditions impacted the region during the
42 ACLOUD campaign. Three key periods were identified: a cold period (CP; 23-29 May), a warm
43 period (WP; 30 May-12 June), and a normal period (NP; 13-26 June). The associated changes
44 of the synoptic conditions lead to sudden variations in the atmospheric thermodynamics
45 properties and cloud structures (Ruiz-Donoso et al., 2020; Wendisch et al., 2023b).

46 **2.1. ACLOUD research flight #19**

47 Flight #19 was performed on 17 June 2017. It lasted more than five hours, two different cloud
48 structures over either sea ice or open ocean surfaces were sampled, hereafter referred to the

1 SI and OO cases. Figure 1a shows the collocated flight tracks of both aircraft on 17 June 2017.
2 Note that there is approximately a seven minute gap between the two aircraft for both cases
3 (Polar 5 is ahead of Polar 6). Polar 5 flew at higher altitudes than Polar 6 (Figure 1b) observing
4 the overall thermodynamic and microphysical structure of the cloud using dropsondes and
5 remote sensing instruments. Polar 6 flew at lower altitudes, i.e., inside the low-level MPCs,
6 following a staircase flight pattern to analyse the profiles of cloud microphysical properties (ice
7 and droplet number concentrations) using *in situ* probes. The instruments installed on the Polar
8 5 and Polar 6 aircraft are summarised by Ehrlich et al. (2019a). All the instruments,
9 measurements and associated uncertainties used in this work are described in the Appendix
10 A.

11 2.2. Overview of the two case studies

12 2.2.1. Synoptic and thermodynamic conditions

13 The synoptic conditions are characterised by the reanalysis ERA-5 produced by the European
14 Centre for Medium-Range Weather Forecasts (ECMWF) The Copernicus Climate Change
15 Service (C3S) has been used to extract meteorological parameters on a $0.25^\circ \times 0.25^\circ$
16 horizontal grid. Figures 2a-c show the 750 hPa geopotential height, relative humidity with
17 respect to liquid water (RH), and air temperature (T) as well as the surface pressure fields on
18 17 June 2017 at 12:00 UTC.

19 Three low (L) pressure systems were present around the ACLOUD region at approximately
20 2.5 km height. The first one was centred over Iceland, the second one over the Baffin Sea west
21 of Greenland, and the third one at the North-East of the Svalbard archipelago (Figure 2a). A
22 weak high (H) pressure system was situated over Northern Europe. These synoptic conditions
23 induced a mixing of two main air masses arriving to the Svalbard archipelago: a cold polar air
24 mass coming from the North Pole (blue arrows) and a temperate air mass from the North
25 Atlantic Ocean via the Norwegian Sea (red arrows). Note that the latter air mass is regularly
26 observed in this region bringing moisture and heat from midlatitudes to higher latitudes
27 (Sorteberg and Walsh, 2008; Tjernström and Graverson, 2009; Woods et al., 2013; Dufour et
28 al., 2016; Yu et al., 2019). The two air masses caused variations in the temperature and relative
29 humidity fields in the vicinity of the ACLOUD region (Figures 2b-c). The RH is on average equal
30 to 87% over the ACLOUD flight #19 area with several saturation spots. RH decreases sharply
31 to about 40% or 50% around the ACLOUD area, southward and the northward. We note that
32 temperature increases by 7°C and RH drops to 52% in the North of the Svalbard archipelago.
33 On the other hand, a cooler air spot present at the West of the Svalbard archipelago is
34 associated with an increase of RH . These thermodynamics conditions induce weather
35 changes, which can promote cloud formation and their persistence (as in Savre et al., 2014).

36 The vertical thermodynamic properties for both case studies are illustrated by the observations
37 of the dropsondes (DS) launched from the Polar 5 aircraft. Two of these dropsondes are
38 specifically used to describe T and RH profiles of both case studies: DS1, which was released
39 over sea ice surface at 11:20 UTC, and DS4 over the ocean at 14:25 UTC (see for both
40 positions Figure 1a). Figure 3 presents the skew- T log- P diagram obtained from the DS1 and
41 DS4 measurements.

42 Figure 3 shows that the surface temperature is equal to -2°C for the SI case, whereas it
43 reaches $+2^\circ\text{C}$ for the OO case. At 950 hPa (corresponding to approximately 500 m), a
44 temperature inversion occurs in both cases reaching up to 860 hPa for SI and up to 920 hPa
45 for OO. An elevated inversion layer is detected for OO reaching from 860 to 820 hPa. The
46 lifting condensation level (LCL) was detected at approximately 980 hPa (around 200 m altitude)
47 for SI, whereas it is slightly higher for OO (at 940 hPa, i.e. around 500 m altitude). Close to the

1 air temperature inversions located at approximately 950 hPa, low-level thin clouds occurred in
2 both SI and OO cases, which is confirmed by the radar reflectivity profiles shown in Section
3 2.2.3. The adiabatic decrease of the temperature below these cloud layers indicates that the
4 boundary-layer is well mixed and that the clouds are thermodynamically coupled to the surface.
5 Moreover, according to the elevated relative humidity ($RH = 95\%$) observed in DS1 and DS4
6 measurements, a second cloud layer was present at higher altitudes (around 2500 m altitude)
7 for both OO and SI cases (see also Section 2.2.3). However, as for the low-level clouds, the
8 base of these mid-level clouds is at a slightly higher altitude in the OO case compared to the
9 SI case.

10 **2.2.2 Air masses origin and aerosol particle properties**

11 Arctic cloud properties are linked to the air mass origin and to the aerosol properties (Gultepe
12 et al., 2000; Gultepe and Isaac, 2002). The air mass origin for both cases is studied using the
13 Computing Advection-interpolation of atmospheric parameters and Trajectory tool (CAT; Baray
14 et al., 2020). CAT is initialised with the wind fields from the European Centre for Medium-
15 Range Weather Forecasts (ECMWF) ERA-5 reanalysis data (Hersbach et al., 2023a,b). The
16 back-trajectories are calculated over a 72 hours duration and a 15 minutes temporal resolution.
17 The surface-atmosphere interface is managed using a topography matrix at a horizontal grid
18 resolution of ≈ 10 km (Bezdek et al., 2013). The advection of air masses is calculated using 3D
19 wind fields with a spatial resolution of 0.25° in latitude and longitude, provided every 3 hours.
20 The number of vertical levels was set to 20 between 1000 hPa and 300 hPa. The initial spatial
21 and temporal coordinates (represented by the black stars in Figure 2d) were defined according
22 to the position of the Polar 6 aircraft at 11:00 UTC and 14:00 UTC for the SI and the OO case,
23 respectively and at an altitude of 500 ± 200 m, which corresponds to in-cloud conditions for
24 both cases according to Figure 3. Figure 2d shows that the air mass of both cases originated
25 from the North of Svalbard, staying over sea ice surfaces, and mostly remained in the ABL.
26 Some trajectory points reach 700 m altitude for the SI case and 950 m in the OO case. Note
27 that in the free troposphere, Arteaga (2023) shows that the air mass towards the Svalbard
28 archipelago is coming from the North-East for the SI case, whereas it is coming from the West
29 for the OO case.

30 For the SI case, the median and interquartile range values of the observed CPC aerosol total
31 particle number concentration ($N_{AP,SI}$) are approximately equal to $(120 \pm 30) \text{ cm}^{-3}$, whereas for
32 the OO case $N_{AP,OO}$ is equal to $(3000 \pm 400) \text{ cm}^{-3}$. This significant difference in N_{AP} is explained
33 by the varying surface conditions as the thermodynamic profiles indicate a well-mixed
34 boundary layer in both cases. The high value over the open ocean may likely be caused by
35 the transport of pollution related aerosols. Note that contrasted N_{AP} values according to surface
36 properties are also discussed in Wendisch et al. (2019, 2023). The CCN number concentration
37 median value estimated for the SI case ($N_{CCN,SI}$) is 9 cm^{-3} , which is quite low but comparable
38 with observations performed at the North of the Svalbard archipelago (Tjernström et al., 2014;
39 Leck and Svensson, 2015). Observations of the CCN number concentration for the OO case
40 ($N_{CCN,OO}$) were not reliable because most of the in-cloud aerosol measurements were affected
41 by inlet freezing during this period. Wendisch et al. (2019) found that the CCN concentration
42 over open ocean surfaces ($N_{CCN,OO}$) was on average equal to 100 cm^{-3} throughout the ALOUD
43 period. Baudoux (2022) estimated that $N_{CCN,OO}$ was on average equal to 28 cm^{-3} when focusing
44 only on measurements performed from 13 to 26 June 2017 under synoptic conditions similar
45 to the OO case. The temporal evolution of the INP concentrations is determined using aerosol
46 particle number size distributions from UHSAS, air temperature and the parameterisation of
47 DeMott et al. (2010). Using this method, the median values estimated for $N_{INP,SI}$ and $N_{INP,OO}$
48 are respectively equal to $8.2 \times 10^{-7} \text{ cm}^{-3}$ and $8.5 \times 10^{-6} \text{ cm}^{-3}$. We note that the estimated INP

1 number concentrations over open ocean (OO case) are higher than over sea ice surfaces (SI
2 case), which is similar to previous studies performed over the same region (Young et al., 2016).

3 **2.2.3 Cloud microphysical properties**

4 Figure 4 shows the temporal evolution of the vertical profiles of the 94 GHz radar reflectivity
5 (Z) derived from measurements with MiRAC (Mech et al., 2019) for both cases. For the SI case
6 (Figure 4a), two types of clouds are present: (i) low-level clouds (200-600 m) with ice
7 precipitation down to the surface and possibly liquid water droplets close to the cloud top. It
8 should be noted, however, that without measurements of depolarization or Doppler spectra,
9 the presence of some drizzle drops cannot be excluded, nevertheless, the LWC of these clouds
10 seems too low to initiate an efficient collision-coalescence process, and hence the radar
11 reflectivity in the precipitation layer can be considered to be dominated by ice particles. (ii) mid-
12 level clouds (1500-3200 m) with vertical bands of high Z , which are related to precipitating ice
13 crystals. For the OO case (Figure 4b), also two types of clouds are observed with cloud bases
14 at higher altitudes than for the SI case: (i) low-level clouds (300-1000 m) with faint precipitation
15 bands below, and (ii) mid-level clouds (2200-3500 m) with stronger precipitation (thick vertical
16 bands of Z below the cloud base). Both radar reflectivity fields are consistent with our analysis
17 of the skew- T log- p diagram given in Section 2.2.1. Figure 4b shows that, unlike in the SI case,
18 the two cloud layers are not concomitant in the OO case. Moreover, the round-trip of the Polar
19 5 aircraft permits the identification of the temporal development of the mid-level clouds with, in
20 particular, the intensification of the precipitation (especially for the OO case).

21 Polar 6 performed *in situ* measurements at altitudes below 1000 m (Figure 1b). The
22 microphysical probes sampled the low-level clouds and the precipitation from mid-level clouds
23 in both cases. Figures 5a-b show the mean cloud droplet size distributions (DSD) derived from
24 the CDP-2 measurements, and the CIP mean particle size distributions (PSD) of hydrometeors
25 with size larger than 75 μm for each flight leg sampled by Polar 6 (Figure 1b) for the SI and
26 OO cases. Ehrlich et al. (2019a) have shown that the ice-PSDs remain quite similar whatever
27 the hypothesis made to calculate the particles diameter, i.e., the maximum diameter D_{max}
28 (Leroy et al., 2016), the equivalent diameter D_{eq} (McFarquhar and Heymsfield, 1996), or the
29 circumpolar diameter D_{cc} (Brown and Francis, 1995). In this study the maximum diameter D_{max}
30 of the ice particles is considered to represent the PSDs and to calculate ice water contents
31 (IWC) (see Appendix A). In the following, we will assume that hydrometeors larger than 75 μm
32 are ice crystals, in line with the processing of CIP data of arctic MPCs presented in Moser et
33 al. (2023). Previous studies have also shown that this hypothesis seems reasonable in most
34 of the low-level Arctic clouds where large hydrometeors are dominated by ice crystals
35 (McFarquhar et al., 2007; Mioche et al., 2017; Korolev et al., 2017; Järvinen et al., 2023).
36 Accordingly, microphysical parameters calculated from the CIP PSDs are considered to be
37 representative of the ice phase (referred hereafter to N_{ice} , IWC and D for ice crystal number
38 and mass concentrations, and maximum diameter, respectively) while parameters obtained
39 from the CDP-2 size distributions characterise liquid water droplets (N_{drop} , LWC).

40 Figure 5 shows the DSDs and PSDs obtained for the different flight legs. For the SI case, the
41 PSDs extend to larger sizes than for the OO. Flight leg 4 reveals that only a few droplets and
42 no ice particles are present at an altitude of 1000 m. Figure 5a shows that the mean PSD
43 obtained for the flight leg 5 is slightly different than for the three other legs: ice particles with
44 diameters < 400 μm are less numerous. The shorter period (only 2 min) of measurement for
45 leg 5 (Figure 1b) might explain this difference for the SI case (the properties of the sampled
46 mixed-phase clouds could have evolved). Regarding the OO case, Figure 5b shows that, even
47 if the DSDs' shapes are quite similar to the SI case, droplets are slightly more numerous (OO:
48 75 cm^{-3} ; SI: 51 cm^{-3}) and have larger sizes (OO: 50 μm ; SI: 40 μm). The higher aerosol
49 concentrations observed for the OO case (see Section 2.2.2) could have affected the droplet

1 microphysical properties. Figure 5b also shows that the ice particles remain smaller and less
2 numerous in the OO case than in the SI case.

3 **2.2.3.1 Cloud radar versus *in situ* probe observations**

4 The instruments deployed on-board Polar 5 and Polar 6 have the advantage of probing the
5 same clouds with different techniques, i.e., remote sensing (MiRAC cloud radar) and *in situ*
6 microphysical probes measurements. We selected the suitable data taking into account both
7 the spatial and temporal position for each leg of the SI and OO cases. Only the periods with
8 in-cloud legs are considered for this study, i.e., legs 1-3 for the SI case and the legs 1-4 for the
9 OO case. Data from leg 5 of the SI case are not considered because this leg is too short (≈ 2
10 min) to correctly define co-localised data.

11 Figure 6 presents the probability density functions (PDF) of the reflectivities measured by the
12 MiRAC radar (Polar 5) and those calculated from observed PSDs and DSDs on board Polar
13 6, using the Self-Similar Rayleigh-Gans Approximation (SSRGA) to realistically consider the
14 distribution of the ice mass within the ice particles (Hogan et al., 2017; Kneifel et al., 2020). To
15 assess the impact of the ice particles size and habit, two different mass-diameter relations
16 $m(D) = a D^b$ relations were used, corresponding to two different hypotheses regarding the
17 degree of riming of the ice aggregates (Tridon et al., 2019a). The first relation, derived by
18 Brown and Francis (1995), assumes unrimed aggregates ($m(D) = 0.012 D^{1.9}$; called hereafter
19 BF95) whereas the second one, which was developed more recently by Leinonen and Szyrmer
20 (2015), assumes slightly rimed aggregates ($m(D) = 0.033 D^{1.94}$; called hereafter LS15). In both
21 cases, D_{\max} was used. This latter relation has been derived from the model for ice aggregation
22 and riming described in Leinonen and Szyrmer (2015). Rimed aggregates are obtained by
23 subsequent aggregation of ice crystals and riming in supercooled liquid water clouds. The
24 LS15 relation used hereafter corresponds to the SSRGA-LS15-B0.2 configuration in the
25 nomenclature given in Tridon et al. (2019a) associated with the fitting method of Ori et al.
26 (2021).

27 For the OO case, Figure 6b clearly shows that the reflectivities calculated from *in situ*
28 measurements considering slightly rimed aggregates (P6-LS15) become more comparable to
29 the reflectivities measured by the cloud radar (P5-MiRAC) than the ones considering unrimed
30 aggregates (P6-BF95). For the SI case, this trend is not as clear. This comparative analysis
31 suggests the presence of slightly rimed aggregates in both cases but with a degree of riming
32 less important in the SI case than in the OO case. A similar conclusion was drawn by Järvinen
33 et al. (2023). To confirm that the riming process occurs in both situations, we analyse the CIP
34 images of ice crystals with sizes larger than $500 \mu\text{m}$ (i.e., the minimum size for a reasonable
35 analysis) for the different in-cloud legs. Slightly rimed aggregates and columns prevailed during
36 each in-cloud leg of the SI situation. We estimated that more than 80% of the ice crystals with
37 size larger than $500 \mu\text{m}$ were affected by riming. Examples of rimed crystal CIP images are
38 shown on Figure 7a. However, for the OO situation, the rare occurrence of ice crystals with
39 sizes larger than $500 \mu\text{m}$ (Figure 5b) does not enable to obtain a representative sample of
40 slightly rimed aggregates. Nevertheless, the few sampled aggregates (Figure 7b) seem to
41 have more rounded shapes in the OO case, suggesting that the riming process is probably
42 more efficient in that case compared to the SI case.

43 **2.2.3.2 Vertical profiles of the MPCs' properties**

44 From the numerous DSDs and PSDs measured along the different legs of the flight, we can
45 calculate the number concentrations of droplets (N_{drop}) and ice crystals (N_{ice}) and deduce the
46 LWC and IWC contents for both SI and OO cases. The mean and the spread values of both
47 concentrations (Figures 8a-b) and LWC and IWC (Figures 8c-d) along the different flight legs

1 (Figure 1b) are used to establish the vertical profiles of the cloud properties for the SI and the
2 OO cases. Moreover, to identify the in-cloud regions, we consider critical thresholds on both
3 the liquid water ($LWC_c \geq 0.01 \text{ g m}^{-3}$) and ice water contents ($IWC_c \geq 5 \times 10^{-5} \text{ g m}^{-3}$) as applied
4 in Mioche et al. (2017) and Dupuy et al. (2018). Note that the calculated IWC varies with the
5 chosen mass-diameter relationship.

6 For the SI case, data collected along flight leg 4 (at $\approx 1000 \text{ m}$) do not characterise in-cloud
7 properties because the mean LWC and IWC values are lower than the LWC_c and IWC_c
8 thresholds (Figure 8c). At this altitude, the mean N_{drop} and $N_{\text{ice}} (< 10^{-6} \text{ cm}^{-3})$ are both negligible
9 (Figure 8a). At $\approx 60 \text{ m}$ (leg 1), we can note that the mean LWC is lower than the LWC_c threshold
10 but both the mean N_{drop} and N_{ice} cannot be neglected (see also Figure 5a). Thus, we assume
11 that the Polar 6 aircraft flew in the precipitation layer (Ehrlich et al., 2019) and close to the
12 cloud base. Within the cloud layer, the N_{drop} is three orders of magnitude higher than the N_{ice} ,
13 and both concentrations remain quite constant along the profile at around 35 drops per cm^3
14 and 0.015 crystals per cm^3 . Moreover, while the LWC remains quite constant, the IWC slightly
15 decreases with increasing altitude (regardless of the mass-diameter relation used in the
16 calculations of the IWC).

17 Figure 8d shows that, according to the LWC_c and IWC_c thresholds, only legs 2-4 (in the altitude
18 range from 200 to 800 m) are inside the clouds for the OO case. Figure 5b shows that the
19 precipitation (at 60 m: leg1) is composed of a few ice crystals. Within the cloud layer, the
20 supercooled liquid water phase is more dominant in the OO case than in the SI case since the
21 LWC is more important while the IWC remains comparable (Figures 8c-d). Moreover, the LWC
22 increases steadily with the altitude especially in the OO case (LWC up to 0.5 g m^{-3} close to
23 cloud top) whereas the IWC remains quite constant with the altitude in both cases, regardless
24 of the m - D relationship. Over open ocean, the estimated liquid water fraction (LWF, defined as
25 the ratio between the LWC and the total water content) is close to 100% in the cloud layers
26 above 300 m and slightly drops to approximately 85% in the lowest cloud layer (60 m). Similar
27 LWF values and trends were also observed in low-level MPCs over the Greenland Sea in late
28 spring by Mioche et al. (2017) (under, however, colder conditions and a southerly air flow).
29 Over sea ice, a comparable LWF trend is observed with maximum values close to 95% above
30 200 m and lower fractions down to 70 % near the cloud base.

31 The two cloud systems observed either over sea ice or over open ocean formed under quite
32 warm Arctic conditions since the temperatures measured inside clouds are between 0°C and
33 -5°C for the SI case and between -3°C and 0°C for the OO case (see Figure 7). However, the
34 vertical structure of the phase partitioning of both cloud systems is similar with supercooled
35 liquid water dominating each layer of the MPCs (Figures 8c-d). Ice formation took place by the
36 heterogeneous nucleation process. The stronger concentration of N_{ice} for the SI case confirms
37 the role of the decreasing temperature for heterogeneous nucleation. Furthermore, as the
38 temperature in the cloud layer for the SI case ranges mainly between -6°C and -5°C (Figure
39 3), we can suppose that also secondary ice production mechanisms such as the Hallett-
40 Mossop process, which is efficient in this temperature range, could also contribute to the ice
41 crystal number concentration (Korolev and Leisner, 2020).

42 **3. Numerical simulations of both MPC cases**

43 **3.1. Model description and strategy of analysis**

44 Simulations of the two MPCs observed over sea ice (SI case) and open ocean (OO case) were
45 done using the non-hydrostatic and compressible WRF model version 3.8.1 (Skamarock et al.,
46 2008), which uses a terrain-following mass vertical coordinate. Physics processes are
47 parameterised and categorised into different schemes to describe microphysics, surface, ABL,

1 and radiation properties. For this study, the simulations for both SI and OO cases use the
 2 following set of parameterisations: the shortwave and longwave radiations follow the Rapid
 3 Radiative Transfer Model for GCMs (RRTMG) scheme based on Iacono et al. (2008) and
 4 Iacono (2011); the surface properties are described by the surface layer scheme of Janjic
 5 (2002) based on the Eta similarity theory (Monin and Obukhov, 1954) combined with the Noah
 6 land-use module (Chen and Dudhia, 2001); the ABL follows the Mellor-Yamada-Janjic (MYJ)
 7 scheme (Janjic, 2002). The two-moment microphysics scheme of Morrison et al. (2009) is used
 8 to describe the cloud microphysical processes (initialising the CCN concentration for both
 9 cases according to the observations: $N_{CCN,SI} \approx 10 \text{ cm}^{-3}$ and $N_{CCN,OO} \approx 100 \text{ cm}^{-3}$). This set of
 10 parameterisations is identical to that used in the WRF-Polar version developed by the Ohio
 11 State University (Hines et al., 2011). However, in our study, the modifications done to the
 12 Noah land-surface model and the sea ice treatment (Hines and Bromwich, 2008; Bromwich et
 13 al., 2009) are not considered. Indeed, they are particularly important for long-term simulations
 14 where the sea ice surface and the snow cover are evolving which is not the case for our cases
 15 that last less than one day. However, to better represent the surface properties, the sea ice
 16 surface albedo was set according to the airborne observations ($\alpha_{SI} \approx 0.79$) performed during
 17 ACLOUD (Stapf et al., 2019a, 2019b, 2020; Becker et al., 2023; Wendisch et al., 2023a).

18 A two-way nested configuration is used with three nested domains at increasing grid spacing:
 19 9, 3, and 1 km. In the horizontal, the numbers of grid points are, from the outermost to the
 20 innermost domain, 120×120 , 274×232 , and 487×430 . The two wider domains are centred
 21 on the Ny-Ålesund station (NyA in Figure 1a) whereas the innermost domain is centred on the
 22 flight position either at 11:00 UTC or at 14:00 UTC in order to respectively study the SI or OO
 23 cases (stars in Figure 2d). For the three domains, the vertical grid consists of 105 non-
 24 equidistant levels (with a model lid at 350 hPa) to have more levels at the altitudes of the MPCs
 25 (mean vertical grid spacing equal to 30-35 m within the first kilometre). The outermost domain
 26 was initialised at 00:00 UTC on 17 June 2017 and forced every 6 hours with the ECMWF ERA-
 27 5 reanalysis. This reanalysis provides the fields of air temperature, specific humidity,
 28 geopotential, and wind components with a spatial resolution of $0.25^\circ \times 0.25^\circ$ in latitude and
 29 longitude for a specified number of pressure levels. Two different simulations using either 21
 30 or 38 pressure levels for the reanalysis data (6 or 9 of them are present in the pressure range
 31 1000-800 hPa, respectively) are performed in order to study the role of the model initialisation.
 32 The three additional pressure levels in the lowest layer of the atmosphere correspond to the
 33 975, 875 and 825 hPa levels. The model settings described above provide the baseline
 34 simulations, which will be referred to as WRF21 or WRF38 for 21 or 38 pressure levels used
 35 in the ERA-5 reanalysis for the two MPC cases. The simulations performed for this study are
 36 summarised in Table 1.

37 **Table 1.** Description of the modelling experiments performed in this study using the ECMWF ERA-5 reanalysis for
 38 WRF initialisation: with either 21 or 38 pressure levels; and with two different parameterisations to describe the ABL
 39 (the MYJ or MYNN3 scheme) and the (MP) microphysics (the Morrison et al. (MORR) or the Milbrandt-Yau (MIYA)
 40 2-moment scheme). Additional sensitivity studies are performed varying the initial CCN concentration $[n]$. Note that
 41 in WRF38* baseline simulations, $[n]$ is 10 cm^{-3} for the SI case and 100 cm^{-3} for the OO case.

| Name | Description |
|--------------------------------|---|
| WRF21 | 21 ERA-5 vertical levels, and with MYJ & MORR physics schemes |
| WRF38 | 38 ERA-5 vertical levels, and with MYJ & MORR physics schemes |
| WRF-BL | As in WRF38, but with MYNN3 ABL scheme |
| WRF-MP | As in WRF38, but with MIYA microphysics scheme |
| WRF-[n]CCN | As in WRF38*, but with CCN concentration equal to $[n] \text{ cm}^{-3}$ |

42 Comparisons of model results with profiling observations are challenging because a model
 43 cannot be expected to reproduce the exact system evolution in space and time. In addition,
 44 the representativeness of the observed profile (DS1 or DS4 dropsonde), the time-height

1 (MiRAC cloud radar), or time-level (*in situ* data leg) is unknown. Therefore, as in Planche et al.
 2 (2019) and Tridon et al. (2019b), we statistically compare the different observations to a large
 3 number of model columns or level-points over the whole simulated cloud for both cases. Thus,
 4 two parallelepipedic volumes with a base of 300 x 140 km² and a vertical extension of 1-1.2
 5 km are defined within the innermost domain. Each of them encompasses the trajectory of the
 6 Polar 6 aircraft for both cases, as represented in Figure 1a.

7 To evaluate the sensitivity of modelled MPCs properties to the representation of the physics
 8 processes, additional simulations are performed using different parameterisations for the ABL
 9 and the microphysical properties (MP). For these simulations, we choose BL and MP schemes
 10 which are commonly used for Arctic cloud studies (such as in Bromwich et al. (2009); Hines et
 11 al. (2011); Xue et al. (2022), among others). Thus, we replace the MYJ scheme with the Mellor-
 12 Yamada-Nakanishi-Niino Level 3 (MYNN3) ABL scheme (Nakanishi and Niino, 2006, 2009)
 13 and the Morrison scheme by the Milbrandt-Yau (MIYA) microphysics scheme (Milbrandt and
 14 Yau, 2005a,b). MYNN3 is a modified version of the MYJ scheme which uses results from large
 15 eddy simulations to derive the expressions of stability and mixing length instead of
 16 observations. In both 2-moments MP schemes, the prognostic variables include number (N)
 17 and mass mixing ratio (q) for all different hydrometeor species (such as rain drop, ice, and
 18 snow). The particle size distribution for each hydrometeor species (x) is described by a gamma
 19 function: $N_x(D) = N_{0,x} D^{\mu_x} e^{-\lambda_x D}$, where D is the diameter, and $N_{0,x}$, μ_x and λ_x are the intercept,
 20 the shape and the slope parameters, respectively. For each hydrometeor species, $N_{0,x}$ and λ_x
 21 are calculated according to Equations 1 and 2 (while μ_x is fixed):

$$22 \quad \lambda_x = \left[\frac{a_x N_x \Gamma(\mu_x + b_x + 1)}{q_x \Gamma(\mu_x + 1)} \right]^{1/b_x} \quad (\text{Equation 1})$$

$$23 \quad N_{0,x} = \frac{N_x \lambda^{\mu_x + 1}}{\Gamma(\mu_x + 1)} \quad (\text{Equation 2})$$

24 Γ is the Euler gamma function, and the parameters a_x and b_x are given by the assumed power-
 25 law mass-diameter relationship ($m(D) = a_x D^{b_x}$) for each hydrometer species. Table 2
 26 summarises the main assumptions of both MP schemes for hydrometeors' representations.
 27 Note that most of the hydrometeor size distributions follow an exponential function since μ_x is
 28 equal to 0. Most of the microphysical processes are based on similar approaches in both MP
 29 schemes. However, even if parameterisations used to represent some of the heterogeneous
 30 ice nucleation mechanisms could differ (see details in MORR and MIYA), there are differences
 31 in the temperature ranges from which the heterogeneous ice nucleation mechanisms are
 32 activated: the deposition/condensation and the contact/immersion freezing mechanisms are
 33 active at $T < -8^\circ\text{C}$ and $T < -4^\circ\text{C}$ in the Morrison scheme whereas they are respectively active
 34 at $T < -5^\circ\text{C}$ and $T < -2^\circ\text{C}$ in the Milbrandt scheme.

35
 36 **Table 2.** Main characteristics of both microphysics schemes used in this study to describe the different hydrometeor
 37 species (x). The definition of the q , N , a , b , and μ variables are given in the text and v , c , r , i , g , h correspond to the
 38 water vapour, cloud droplet, rain drop, ice, graupel, and hail species, respectively. ρ_x corresponds to the density for
 39 each species. Note that μ_c follows Martin et al. (1994) in MORR scheme.

| | Morrison scheme (MORR) | Milbrandt-Yau scheme (MIYA) |
|---|---|---|
| Mass variables | q_x for $x \in \{v, c, r, i, s, g\}$ | q_x for $x \in \{v, c, r, i, s, g, h\}$ |
| Number variables | N_x for $x \in \{r, i, s, g\}$ | N_x for $x \in \{c, r, i, s, g, h\}$ |
| m-D coefficients | $a_x = \frac{\pi}{6} \rho_x$; $b_x = 3$ for $x \in \{c, r, i, s, g\}$ | $a_x = \frac{\pi}{6} \rho_x$; $b_x = 3$ for $x \in \{c, r, s, g, h\}$ & $a_i = 440 \text{ kg m}^{-3}$ |
| Shape parameter | $\mu_x = 0$ for $x \in \{r, i, s, g\}$ $\mu_c = \text{fct}(N_c, T, p)$ | $\mu_x = 0$ for $x \in \{r, i, s, g, h\}$ & $\mu_c = 3$ |

40

1 3.2. WRF baseline simulations

2 In Figure 8, results from WRF21 and WRF38 simulations for both SI and OO cases are already
3 included. In WRF experiments, the microphysical properties are determined by selecting a
4 sample of points within the parallelepipedic volume matching with the P6 flight path (leading
5 typically to more than 200 points in total). Temporally, we consider all the model outputs every
6 5 min between 11:00 and 12:00 UTC for the SI case and between 14:00 and 15:00 UTC for
7 the OO case. Moreover, from the WRF experiments, the LWC is calculated using the mass
8 mixing ratios of both cloud (q_c) and rain (q_r) species while the IWC is calculated using the mass
9 mixing ratios of both ice (q_i) and snow (q_s) species ; the other ice species in MORR are empty
10 for the two studied MPC cases. Indeed, the simulated cloud LWC is too small and the
11 corresponding cloud droplet spectra are too narrow (Figure 5a-b for the SI and the OO case,
12 respectively) to activate the collision-coalescence process permitting the formation of
13 raindrops which are important in the graupel formation. Regarding the concentration profiles,
14 the sum of N_c and N_r is used to determine N_{drop} while the sum of N_i and N_s is used for N_{ice} . Note
15 that N_c , which is not a prognostic variable in the Morrison scheme, is fixed according to the
16 N_{CCN} values used to initialise both cases (Section 3.1). Consequently, N_{drop} profiles in Figures
17 8a-b depict a constant value of 10 cm^{-3} for SI and 100 cm^{-3} for OO in both WRF21 and WRF38
18 simulations.

19 The median LWC profile in WRF38 is in better agreement with the observations than WRF21
20 for both SI and OO cases (Figures 8c-d). The observed LWC remained significantly below
21 values assuming adiabatic lifting while all modelling results shown hereafter are very close to
22 adiabatic lifting conditions (see also Figures 11a-b where the vertical LWC profiles both
23 WRF38 SI and OO are depicted in a linear scale). However, neither the vertical evolution nor
24 the amount of the IWC are well reproduced in both WRF21 and WRF38 experiments for the
25 SI case. WRF38 better hits the observed IWC, especially in the first 200 m, for the OO case.
26 The simulated median IWC profile is closer to the observed IWC estimated using the BF95 m -
27 D relationship (Figure 8d). This, however, is in contradiction with the results presented in
28 Section 2.2.3 where it was found that radar reflectivity was better reproduced when the LF15
29 m - D relationship for rimed particles was used. Despite this, the simulated median IWC profile
30 in WRF38 is within the spread interval of the observations. Figure 8d shows that the simulated
31 OO cloud top is not well reproduced in WRF38 and WRF21 since the LWC and IWC sharply
32 decrease at 650 m altitude while the observations suggest a cloud top at ≈ 900 m (leg 5); this
33 is due to drier conditions in simulations than in observations (see also Figure 9b). N_{drop} profiles
34 (Figures 8a-b) reflect the CCN number concentrations initially chosen for SI and OO cases.
35 The selected number of 100 CCN cm^{-3} overestimates the N_{drop} observations for the OO case
36 by 20-30%. For the SI case, 10 CCN cm^{-3} underestimates the observations for N_{drop} by a factor
37 of 2-4. N_{ice} is underestimated in WRF21 as well as in WRF38. This underestimation is around
38 one order of magnitude for the OO case whereas it reaches approximately two orders of
39 magnitude for the SI case.

40 This disagreement will further be investigated by exploiting the dropsonde data at the altitudes
41 where the MPCs formed. Figures 9a-b compare the mean vertical evolution of the
42 thermodynamics properties simulated in WRF21 and WRF38 with the profile of the observed
43 air temperature T and dew point temperature T_d . Simulated profiles of T and T_d are obtained
44 averaging the 20×20 model columns centred on the position in latitude and longitude of each
45 dropsonde (Figure 1) for a one-hour period for the time of the dropsonde releases, *i.e.*, from
46 10:30 to 11:30 UTC for the SI case and from 13:30 to 14:30 UTC for the OO case.

47 According to Figure 9a, the LCL obtained in both WRF21 and WRF38 are comparable to the
48 observations for the SI case. However, even if the vertical evolution of T_d is similar to the

1 observations up to 950 hPa, it is overestimated by $\approx 1.5\text{-}2^\circ\text{C}$ while the T is overestimated by \approx
2 $1\text{-}1.5^\circ\text{C}$ close to the surface in both simulations. These warmer conditions could explain the
3 weak simulated IWCs. As the vertical variations of the potential temperature (θ) between the
4 surface and the cloud base are below 0.5°C , observations and simulations reveal a coupled
5 cloud-surface situation as proposed by Gierens et al. (2020) and Griesche et al. (2021). Also,
6 the T -inversion that is present at a slightly higher altitude in WRF21 than in WRF38 justifies
7 the difference in the altitude of the cloud top visible in Figure 8c for the SI case. The altitude of
8 the T -inversion in the observations (located just above the isotherm layer) suggests a cloud
9 top at higher altitudes than in both experiments, *i.e.*, between flight legs 5 and 4 (see Figure
10 1b). For the OO case, the vertical profile of T is well reproduced close to the surface by both
11 WRF experiments while modelled T_d is overestimated by $\approx 2^\circ\text{C}$ (Figure 9b). The LCL is
12 therefore lower in the simulations than in the observations. As for the SI case, the adiabatic
13 conditions indicate the presence of surface-coupled clouds. At higher altitudes, T_d is better
14 estimated by the simulations but the T -inversion is more marked and T is overestimated by \approx
15 2°C in the pressure range from 925 to 850 hPa. These differences in the vertical evolution of
16 T impact the altitude of the cloud top as well as the LWC and IWC (Figure 8d). Based on our
17 analyses presented in Figures 8 and 9, the WRF38 experiment will be considered hereafter as
18 our reference experiment.

19 Additional comparisons between observations and baseline simulations (*i.e.*, WRF38) are
20 performed on the vertical properties of the MPCs for both cases using a statistical approach.
21 Figure 10 shows the altitude-dependent probability density functions (a-PDF) of reflectivities
22 measured by the MiRAC 94 GHz cloud radar.

23 In order to focus on the MPCs properties, we excluded MiRAC data from 11:35 to 11:45 UTC
24 in our analysis to avoid the precipitation of the mid-level clouds for the SI case (see Figure 4a).
25 Similarly, we selected only MiRAC data from 14:15 to 14:45 UTC to avoid the rainy periods of
26 the mid-level clouds for the OO case (see Figure 4b). PDFs of radar reflectivities calculated
27 from *in situ* measurements (along in-cloud legs done by the P6 aircraft, Figure 6) are also
28 shown in Figure 10. The 94 GHz radar reflectivities are calculated with the Cloud-resolving
29 model Radar SIMulator (CR-SIM, Oue et al., 2020) from the WRF simulations. It is a forward-
30 modelling post-processing tool that emulates various remote sensing products in accordance
31 with assumptions used in the microphysics scheme, *i.e.*, the Morrison scheme for both WRF38
32 baseline experiments (Table 2). The WRF outputs are selected with the same method used
33 for the LWC and IWC analyses detailed in Figure 8.

34 Figures 10a-b show different vertical evolutions of the median a-PDF reflectivities of the MiRAC
35 observations for both cases. For the SI case, it increases from -22 to -12 dBZ towards the
36 ground whereas, for the OO case, it reaches a maximum of -20 dBZ at an altitude of 800 m
37 and then slightly decreases to -25 dBZ at the cloud base. These vertical trends are consistent
38 with *in situ* measurements which have shown that hydrometeors are larger in the SI case
39 (Figure 5). In WRF38, the vertical evolution of the median a-PDF of the modelled reflectivities
40 is comparable to the observations for both cases (Figures 10c-d). However, the reflectivity
41 fields are more homogeneous in the model than in the MiRAC observations (see Q1-Q3
42 spread). Also, Figure 10d confirms that MPCs simulated for the OO case are less high than
43 observed (due to the position of the T -inversion; Figure 9b).

44 Figure 10 shows that radar reflectivities modelled in WRF38 slightly underestimate the cloud
45 radar MiRAC observations for both cases (median difference < 4 dB). This underestimation
46 might be explained by the fact that the simulated ice particle spectra underestimate the
47 observed particle number but give a wider spectrum with larger particles, which contribute
48 essentially to the reflectivity. Table 2 shows that the modelled ice PSDs are prescribed

1 according to exponential distributions ($\mu = 0$) in MORR whereas the observed PSDs are rather
 2 defined according to gamma distributions (Figure 5).

3 3.3 Impact of the atmospheric boundary layer and microphysical parameterisations

4 The WRF38 baseline experiment provides reasonable results compared to the observations
 5 with some discrepancies such as the underestimation of the ice phase and the altitude of the
 6 cloud top. To evaluate how these MPC parameters can be impacted by the physics
 7 parameterisations used in our modelling set-up, we performed sensitivity studies using other
 8 representations for the boundary layer (BL) and the microphysical properties (MP), as
 9 described in Section 3.1. These alterations with respect to the WRF38 set-up are summarised
 10 in Table 1. Figure 11 represents the median vertical profiles of the LWC and IWC obtained in
 11 WRF-BL and WRF-MP for both cases. We can note that the trend of LWC for WRF-MP in
 12 Figures 11a and 11b corresponds to adiabatic lifting.

13 LWC and IWC simulated with WRF-BL are similar to the values found in WRF38 but both liquid
 14 and ice water phases extend on thicker layers and are observed at higher altitudes. For the SI
 15 case, the cloud liquid water phase is shifted upwards by approximately 200 m and the cloud
 16 ice reaches up to 800 m altitude (Figure 11). Figures 11b and 11d show that the impacts are
 17 opposite for the OO case since IWC is shifted upwards by approximately 200 m whereas the
 18 liquid water phase extends over 500 m, *i.e.*, 100 m more than in WRF38. We can note that
 19 LWC at cloud top (Figure 11b) reaches 30 to 50 m higher than IWC (Figure 11d). In fact,
 20 according to Figure 9d, the temperature becomes positive just below the 900 hPa level in WRF-
 21 BL causing the instantaneous melting of the ice crystal to liquid droplets at cloud top. The
 22 modifications of the vertical profiles of the condensed water for the two cases can be induced
 23 by changes in surface sensible (F_{sen}) and latent (F_{lat}) fluxes and in the thermodynamics
 24 structure within the ABL. Indeed, the mean F_{lat} increases by around 20% in WRF-BL for both
 25 cases, while a significant reduction in the mean F_{sen} of -25% only occurs for the SI case. Table
 26 3 summarises the mean F_{sen} and F_{lat} obtained for each WRF-BL experiment. Note that the
 27 surface fluxes in the OO case are 5-6 times stronger than in the SI case. From Figure 9, one
 28 can see that the air temperature at the surface is 1°C warmer in WRF-BL than in WRF38 for
 29 the SI case. The lower atmospheric layer is more humid up to 910 hPa where a more marked
 30 T -inversion is present, *i.e.*, at higher altitude than in WRF38 as well as in the observations (see
 31 Figure 9c). For the OO case, the T -inversion is also located at a slightly higher altitude (\approx 10-
 32 20 hPa) than in WRF38 (Figure 9d). Below this point, T and T_d have a similar vertical gradient
 33 even if they are stronger than in WRF38. Thus, the MYNN3 scheme allows the development
 34 of stronger turbulent mixing impacting the cloud top inversion layer and/or its displacement to
 35 higher altitudes.

36 **Table 3.** Mean surface sensible (F_{sen}) and latent (F_{lat}) fluxes simulated in WRF38 and WRF-BL for both SI and OO
 37 cases. The numbers in brackets indicate the respective relative differences between WRF-BL and WRF38.

| | SI case | | OO case | |
|--------------------------|---------|---------------|---------|----------------|
| | WRF38 | WRF-BL | WRF38 | WRF-BL |
| F_{sen} ($W m^{-2}$) | 4.94 | 3.67 (-25.7%) | 21.81 | 21.44 (-1.70%) |
| F_{lat} ($W m^{-2}$) | 3.38 | 4.10 (+21.3%) | 26.03 | 31.10 (+19.5%) |

38 Figure 11 also represents the vertical profiles of the LWC and IWC obtained in WRF-MP for
 39 both cases (see Table 1). In that WRF microphysics experiment, not only the quantities for
 40 LWC and IWC change but also their vertical profiles. For the SI case, the ice phase is more
 41 important than in WRF38 by a factor of 2 and extends up to 750 m altitude (\approx 150 m higher
 42 than in WRF38) and becomes more comparable to the observations (see Figure 11c). The
 43 liquid phase simulated in WRF-MP also extends up to 750 m and reaches a maximum of 0.56

1 g m⁻³ at 650 m altitude, *i.e.*, an amount that is twice the one in WRF38 or in the observations
2 (Figure 11a). So, with the MIYA microphysics scheme (used in the WRF-MP experiment), both
3 LWC and IWC become more important than in WRF38 for the SI case. This is due to changes
4 in the temperature and humidity profile: the *T*-inversion is located at higher altitude (as in WRF-
5 BL) and also the lowest levels of the atmosphere are more humid and warmer (0.5-1°C) in
6 WRF-MP compared to the WRF38 experiment and the observations (Figures 9a,c). The liquid
7 water fraction (LWF) estimated for WRF38 is higher ($\approx 90\%$) than WRF-BL ($\approx 70\%$) in the
8 lowest layers for SI case. For the OO case, the changes in the vertical profile of LWC and IWC
9 are small in WRF-MP compared to WRF38 (Figures 11b,d) since only the ice phase appears
10 more important in the lowest atmosphere and the maximum of the liquid phase increases
11 around 20% at the cloud top. At this altitude of 925 hPa, more water vapour is available
12 according to the thermodynamics conditions (see Figure 9d) while they are similar to WRF38
13 conditions at lower altitudes. For the OO case, the vertical distribution of water is almost the
14 same in both cases.

15 The MIYA microphysics scheme (used in the WRF-MP experiment, see Table 1) implies more
16 ice, especially in the SI case. This is related to the different temperature thresholds used in
17 MORR and MIYA microphysics schemes in order to activate the heterogeneous ice nucleation
18 mechanisms. Indeed, all of the ice formation mechanisms parameterised in MIYA are activated
19 at warmer temperatures than in MORR (see Section 3.1). Thus, these assumptions can have
20 an important impact on the SI simulations where in-cloud temperatures are flirting with the
21 threshold values.

22 **4. Sensitivity to CCN concentration**

23 An additional sensitivity study is performed using the WRF38 baseline simulations for the SI
24 and the OO cases (defined in Section 3.2) to investigate the effects of the CCN concentration
25 (N_{CCN}) on MPCs' microphysics properties. In that context, several WRF experiments are done
26 (see Table 1) where the cloud droplet concentration (N_c) is set equal to CCN concentrations
27 ($[n]$) as observed in various Arctic or marine environmental conditions (*e.g.* Planche et al.
28 (2017); Wendisch et al. (2019); Baudoux (2022)). Figure 12 shows the median vertical profiles
29 of LWC and IWC for the different scenarios.

30 For the SI case, an increase by a factor of three in the CCN concentration (from 10 cm⁻³ in
31 WRF-10CCN to 30 cm⁻³ in WRF-30CCN) impacts the LWC as well as the IWC (Figures 12a,c).
32 Indeed, the LWC increases by a factor of 2 while the IWC increases from 1.5 x 10⁻⁴ g m⁻³ to 5
33 x 10⁻⁴ g m⁻³. The vertical distribution of the liquid water phase is also modified since it extends
34 over 600 m (*i.e.*, 100 m more than in WRF38) (Figure 12a). Consequently, with an increasing
35 CCN perturbation, the liquid water phase becomes more important and extends over a deeper
36 layer. Stronger changes in the CCN concentration modify the thermodynamic properties close
37 to the surface and induce modifications in the MPC development. Indeed, in all WRF
38 experiments with $N_{CCN} \geq 100$ cm⁻³ the *T*-inversion is shifted upwards since it is located around
39 150 m higher than in WRF38 (not shown). Note that an increase of 2.5 times in the CCN
40 concentration from 100 cm⁻³ to 250 cm⁻³ only induces a slight increase (+5%) of the liquid
41 phase and has almost no effect on the ice phase (see WRF-100CCN and WRF-250CCN in
42 Figures 12a,c).

43 For the OO case, with an increase in the CCN concentration by a factor of three (from 10 to
44 30 cm⁻³), the liquid phase increases by a factor of 2.5 and extends over a deeper layer while
45 the ice phase increases by a factor of 10 (Figures 12b and 12d). These changes in the IWC
46 are more important than in the SI case for an identical variation in the initial CCN concentration.
47 Increasing the CCN concentration to 100 cm⁻³, the LWC continues to increase and the cloud

1 top becomes higher. Note that in all sensitivity tests with CCN concentrations higher than \geq
2 250 cm^{-3} , the total water content remains similar. As in the SI case, there is a critical CCN
3 concentration from which the ABL seems “to be saturated” for the OO case. Moreover, the
4 thermodynamic properties are quite similar in all experiments, except in WRF-10CCN, where
5 the T -inversion does not evolve vertically and remains at an altitude of 300 m.

6 The sensitivity of cloud microphysics properties to CCN concentration is more important for
7 the SI case than for the OO case. As in Eirund et al. (2019), an increase of the CCN
8 concentration successively increases LWC and IWC. However, at a critical concentration, the
9 LWC and IWC no longer increase for both SI and OO cases. Moreover, the higher the CCN
10 concentration is, the deeper the cloud is.

11 **5. Discussion**

12 During the ACLOUD campaign two shallow cloud layers ($< 700 \text{ m}$) were probed, one over sea
13 ice surface (SI) at temperatures around -5°C , and another over the open ocean (OO) under
14 slightly warmer conditions around -2°C . LIDAR and RADAR observations indicate that the
15 cloud field over sea ice typically ranged from the surface up to 500 m while clouds over open
16 ocean were more elevated with a cloud base close to 200 m and a cloud top of around 900 m
17 (Figure 4). *In situ* measurements show that the LWC reaches 0.4 g m^{-3} at 400 m over the open
18 ocean while a maximum of 0.2 g m^{-3} is obtained in cloud layers over sea ice at the same
19 altitude level. LWC still increases in the OO case up to 0.5 g m^{-3} at 500 m (Figure 8d) while
20 LWC in the SI case at these levels strongly decreases, indicating the top of the cloud. We
21 presume that a strong entrainment with sub-saturated air from altitudes above the cloud top
22 reduced the LWC in the SI case. In addition, in the SI case, the vertical structure of the
23 temperature measured by the dropsonde DS1 (Figure 3) reflects a wet adiabatic profile
24 indicating a well-mixed structure over the entire cloud layer. In contrast to that, the observed
25 temperature profile (DS4) in the lower 400 m of the OO case is dry-adiabatic, justifying the
26 observed LWC of 0.4 g m^{-3} for adiabatic ascent between 200 and 400 m.

27 Airborne measurements indicate that the aerosol particle concentrations differed significantly
28 between both situations, suggesting that the CCN concentration over SI (with 10 cm^{-3})
29 represents a cleaner environment than clouds encountered in the OO case (with 100 cm^{-3}).
30 This strong discrepancy could not be confirmed by measurements of the droplet number, which
31 typically counted 30 droplets/ cm^3 in the SI case, and only 70 droplets/ cm^3 in the OO case. The
32 number of ice crystals was not correlated with the differences in aerosol concentration: while
33 20 crystals per litre were counted in the SI case, only 5 crystals per litre were detected in clouds
34 over the open ocean. We can speculate that the lower temperatures in the SI clouds intensified
35 ice particle formation due to more efficient heterogeneous nucleation. The colder temperatures
36 of the SI case also probably favoured the formation and the growth of larger crystals up to 2
37 mm, while ice particles sizes remained below 0.5 mm in the OO case (Figure 5). The presence
38 of large ice crystals is confirmed by observations of the cloud radar reflectivity Z at 94 GHz.
39 While Z remains below -20 dBZ in the cloud layers over the open ocean, it is higher, ranging
40 from -20 to 0 dBZ in the SI case.

41 After an integration time of 12 to 14 h, simulations with the WRF model reasonably reproduced
42 the low Arctic cloud layers observed on 17 June 2017 over sea ice and open ocean. Model
43 results for cloud layer depth, LWC and drop number are quite comparable with the
44 observations. However, IWC and ice crystal number are significantly underestimated.
45 Furthermore the model could not represent the mid-level cloud layer, which was observed by
46 remote sensing instruments between 1500 and 3500 m in both cases (Figure 4). This cloud
47 layer could affect the turbulent structure of the ABL by reducing the cloud-top cooling of the

1 lower cloud layer and hence its turbulence and entrainment rates as shown by Chechin et al.
2 (2023). A seeder-feeder mechanism could also take place, influencing the ice crystal
3 concentration and mass of the lower cloud layer. These processes could be responsible for a
4 part of the observed microphysical discrepancies but were not further investigated in the
5 present study.

6 In a first step, the role of the vertical resolution of the large-scale data, which provide initial and
7 boundary conditions for the model, was tested. Simulations with 21 vertical levels were
8 compared with those using 38 levels. The low-level cloud layer formed in both configurations.
9 However, with additional levels close to the surface, clouds could form at lower altitudes
10 causing a slight increase of LWC in the 400 m level, thus in better agreement with the
11 observations. Model results for ice crystal number concentration N_{ice} and IWC are only
12 marginally affected by the change of the vertical resolution. Most striking is the comparison
13 between the simulations and the observations of N_{ice} . Modelled ice crystal numbers are 100
14 times lower than observed numbers in the SI case and 50 times lower than observations in the
15 OO case (Figure 8). Cloud imaging probe measurements are subject to potentially significant
16 errors when estimating concentrations and the shape of small hydrometeors. On the one hand,
17 assuming that all the hydrometeors with size larger than 75 μm are ice crystals could result in
18 an overestimation of N_{ice} and to a lesser extent IWC. On the other hand, the total ice number
19 concentration is probably underestimated since only crystals with size larger than 75 μm are
20 considered in the CIP data analysis. Observational results for the IWC are also uncertain as
21 this quantity strongly depends on the m - D relationship applied to the particle number
22 distributions and to the degree of riming of the ice particles (Figures 8 and 10). The resulting
23 IWC range in the SI case is typically from 1 to 5 mg m^{-3} and from 0.1 to 1 mg m^{-3} in the OO
24 case. These values are nonetheless an order of magnitude higher than the maximum IWC
25 (below 0.2 mg m^{-3}) found by the model, especially for the SI case. We can see from these
26 results that the formation of ice crystals and the resulting IWC are significantly underestimated
27 by the microphysics of the model. To a certain extent, the underestimation of the modelled
28 IWC can also be attributed to the warmer air, simulated in the first 500 m for all modelled cases.
29 This underestimation is more pronounced in the SI case, where the simulated temperature in
30 the lower 300 m was up to 1.5 $^{\circ}\text{C}$ higher than the observed one.

31 Significant changes in the vertical structure of the simulated boundary and cloud layer
32 occurred, after replacing the MYJ ABL scheme with the model of Nakanishi and Niino (2009)
33 (MYNN3). The use of the MYNN3 scheme caused a significant vertical shift of the cloud layer
34 in both cases (see WRF-BL in Figure 11). The cloud top for the SI case extends from 450 to
35 750 m and for the OO case from 400 to 800 m. All microphysical properties remained quite
36 similar in the cloud layer as in previous simulations using the MYJ scheme (WRF38 in Figure
37 11). The lifting of the cloud top is accompanied by the lifting of the temperature inversion
38 (Figures 9c and d). Below the inversion, the cloud evolution produced a wet adiabatic lapse
39 rate, and the temperature increased from the surface up to the cloud top compared to the MYJ
40 results. This warming in the ABL can be attributed to the increase in surface latent heat flux
41 (Table 3), which increased in both cases by 20% for simulations with the MYNN3 scheme. We
42 can speculate that this modified evolution in the ABL is due to the different parameterisation
43 of turbulence used in the MYNN3 scheme.

44 Heterogeneous ice nucleation is the dominant microphysical process for crystal formation in
45 the temperature range slightly below 0°C . All simulation results discussed until here concerned
46 the Morrison scheme, wherein heterogeneous nucleation is triggered for temperatures below
47 -4°C . The consequence of a shift to warmer temperatures for the cloud layer was studied using
48 the microphysics scheme MIYA wherein heterogeneous nucleation begins at -2°C . For the
49 simulation with MIYA microphysics over open ocean no remarkable modifications occurred in

1 the profiles of LWC and IWC (i.e. similar to the ones shown on Figure 11). The ABL structure
2 (Figure 9d), is also almost identical with temperature profiles close to the ones obtained on
3 Figure 9d with the Morrison scheme. This result is not surprising as the temperatures in the
4 simulated OO case remain largely above -2°C . Under colder conditions, such as those
5 encountered in the sea ice case, the magnitude of LWC and IWC as well as the cloud layer
6 depth increased significantly. Due to the amplified release of latent heat by water vapour
7 condensation, temperatures in the cloud became almost 1°C warmer and the cloud top height
8 increased by 200 m. As the increase of LWC in the MIYA scheme dominates the results in the
9 SI case, it becomes obvious that other cloud parameterisations than heterogeneous ice
10 nucleation influence these model results. Thus, simulations with the MIYA microphysics do not
11 provide unambiguous information on the role of the temperature threshold for heterogeneous
12 ice nucleation.

13 The microphysics scheme of Morrison is initialised with a fixed CCN value, which corresponds
14 to the number of cloud droplets that is kept constant along the simulation. Variations of the
15 CCN number (Figure 12) show that an increasing CCN concentration leads to more LWC and
16 clouds become deeper. The same result can be detected for the vertical profiles of IWC, even
17 though the trend is less pronounced. This unexpected behaviour of the LWC with changing
18 cloud drop number is basically due to the fact that the total drop number determines,
19 consecutively to LWC, the shape (μ_c ; Table 2) of the gamma size distribution (Martin et al.,
20 1994). For a given LWC of 0.2 g m^{-3} and droplet numbers of 10, 30, 50, 100, or 200 per cm^3
21 (typical values encountered in our sea ice case), the resulting gamma distribution corresponds
22 to an effective radius of 15.72, 10.89, 9.22, 7.45 or $6.17\text{ }\mu\text{m}$, respectively (Figure 13a). Thus,
23 the lower the number concentrations the more spread the modelled droplet spectrum has. The
24 most important consequence of this is that fall speed and auto-conversion rate both increase
25 and enhance the precipitation formation when low droplet concentrations are simulated (as in
26 Khairoutdinov and Kogan (2000); Planche et al. (2015), among others). In this example, for
27 spectra with 10 drops per cm^3 the corresponding mass-weighted fall speed of the droplets is
28 almost 10 times higher and the auto-conversion rate is 200 times stronger than for spectra with
29 200 drops per cm^3 (Figure 13b). Thus, the increase of LWC and cloud depth encountered in
30 the simulations for increasing CCN numbers could be attributed to the overestimation of
31 precipitation caused by the use of a prescribed gamma function.

32 **6. Conclusions and outlook**

33 The main objective of this work was to investigate changes in cloud microphysical and ABL
34 thermodynamic properties with surface type. To do this, we compared the modelling results
35 with a large number of observations (*in situ* and remote sensing) performed during the
36 ALOUD flight #19 where two MPC systems were observed over sea ice and open ocean.
37 Both MPCs evolved in a quite warm environment (between -4 and 0°C) and are characterised
38 by a dominating liquid phase. The impact of particle pollution on the cloud parameters was
39 also investigated by varying the CCN/droplets number concentration. This study also enabled
40 us to assess the WRF model's performance in accurately reproducing Arctic MPCs
41 microphysical structure over different surfaces.

42 For both cases, the WRF model underestimates the observed ice crystal number
43 concentrations and the associated IWC using the microphysics schemes MORR or MIYA.
44 Indeed, ice crystal number concentrations are underestimated by around one or two orders of
45 magnitude for the OO case and the SI case respectively. Temperatures in WRF simulations
46 are slightly higher (about 1 to 2°C) than the observed ones, affecting that ice formation via the
47 heterogeneous ice nucleation process becomes quite unimportant. However, simulated radar
48 reflectivity reasonably compares (median difference $< 4\text{ dB}$) with observations because the

1 predefined exponential function for the ice particle distribution describes wider spectra with
2 larger particles than observed (which are essential to the reflectivity).

3 Changing the number of levels in the vertical profiles of the ECMWF ERA-5 data used to
4 initialise the simulations affects both the altitude of the MPC layer and the LWC while modifying
5 the ABL scheme (MYJ or MYNN3) essentially affects the altitudes of the cloud top and base
6 for up to 200 m. Thus, WRF better reproduces the two Arctic MPCs studied in this work when
7 the number of ECMWF ERA-5 levels is higher close to the surface and with the MYJ scheme.

8 Increasing the CCN and thus the droplet number concentrations induce deeper clouds (up to
9 approx. 200 m) and larger LWC. Also, the ice amount increases from $2 \times 10^{-4} \text{ g m}^{-3}$ to 7×10^{-4}
10 g m^{-3} when CCN is increased by a factor of 10 but remains significantly smaller than the liquid
11 amount (by 3 orders of magnitude). Actually, due to the gamma function used to represent the
12 drop size distributions, the effective droplet radius is reduced by a factor of 2, impacting
13 strongly the efficiency of the warm rain processes (i.e., lower auto-conversion rate since it
14 decreased by 2 orders of magnitude). This influences the altitude of the T-inversion inducing
15 deeper cloudy conditions where ice can also be formed. This results confirm findings of
16 Stevens et al. (2018) highlighting that the representation of the cloud droplet size distribution
17 and the autoconversion scheme should be improved in models and constrained by
18 observations to correctly estimate aerosol-cloud interactions in the Arctic.

19 In the future, it could be interesting to assess the performances of other mesoscale models
20 (such as MetUM or ICON) in reproducing Arctic MPCs microphysical structures. Moreover,
21 studies with a newer version of the WRF model (than v3.8.1) will benefit from improved
22 approaches to represent microphysical processes in MPC systems, such as the treatment of
23 the prognostic aerosols (Thompson and Eidhammer, 2014), of the riming process (P3 scheme;
24 Morrison and Milbrandt, 2015) and of the ice habit (ISHMAEL scheme; Jensen et al., 2017). In
25 another approach, we plan to simulate the two studied MPC systems studied with a 3D
26 mesoscale model using the DEtailed SCAvenging Model (DESCAM; Flossmann and Wobrock,
27 2010; Planche et al., 2010, 2014) bin microphysical scheme (where the size distributions for
28 drops and ice crystals are not predefined and the supersaturation is explicitly computed for
29 each time step (i.e., no saturation adjustment assumption is used)). Then, studies that are
30 more extensive are possible to quantify the role of the aerosol particles on the liquid and the
31 ice phases of the different MPCs.

32 **Appendix A**

33 The instruments and measurements described hereafter are used for the analysis of the
34 research flight #19 (considered in this study):

35 i. *Vertically pointing MiRAC 94 GHz cloud radar (Polar 5)* (Küchler et al., 2017) provides the
36 radar reflectivity Z_e (in $\text{mm}^6 \text{ m}^{-3}$) and the reflectivity factor $Z = 10 \log_{10} Z_e$ (in dBZ) with
37 an uncertainty of 0.5 dBZ (Mech et al., 2019). The data set is available via Kliesch
38 and Mech (2019);

39
40 ii. *Airborne Mobile Aerosol Lidar (AMALi) system (Polar 5)* (Stachlewska et al., 2010)
41 measures the cloud top height. The processed data of AMALi (Neuber et al., 2019)
42 were combined with the MiRAC dataset to characterise the vertical structure of the
43 MPC systems;

44 iii. *Dropsondes (Polar 5)* were operated using the AVAPS (Advanced Vertical Atmospheric
45 Profiling System; Ikonen et al., 2010) providing vertical profiles of air temperature,
46 humidity, pressure, and horizontal wind vector between the typical flight altitude of 3
47 to 4 km and the surface with a vertical resolution of 5 m (Ehrlich et al., 2019b);

- 1
2 iv. *Cloud Droplet Probe (CDP-2) (Polar 6)* is a forward-scattering optical spectrometer
3 operated with anti-shatter tips to limit artefacts caused by the shattering of ice crystals
4 on the probe inlet. CDP-2 measures the droplet number size distribution (DSD) over
5 the size range from 2 μm to 50 μm (with a 1 to 2 μm bin width) (Lance et al., 2010).
6 Microphysical parameters such as the liquid water content (LWC), the number
7 concentration of droplets (N_{drop}), and the droplet size are derived from the measured
8 DSDs. Systematic uncertainties on these quantities are estimated at 10 to 30% for
9 N_{drop} , 10 to 50% for droplet sizing and 20% for LWC (Baumgardner et al., 2017).
10 Statistical uncertainties in droplet number concentration are typically lower than a few
11 %. CDP-2 products and DSD data are published in the PANGAEA database in Dupuy
12 et al., 2019.
- 13
14 v. *Cloud Imaging Probe (CIP) (Polar 6)* is an optical array probe which acquires the two-
15 dimensional black and white images of the hydrometeors as they pass through the
16 laser beam of the instrument. The shadow cast by the cloud particle is recorded on a
17 photodiode array and analysed to provide the hydrometeor size and shape
18 (Baumgardner et al., 2011). Total cloud particle size distributions are computed from
19 the hydrometeor images from 75 to 1550 μm with a 25 μm resolution (the first two
20 size bins are removed due to large measurement uncertainties in the 25-75 μm size
21 range). Shattering and splashing of hydrometeors on the instrument tips are removed
22 based on image processing and inter-arrival time statistics. When the area of the
23 hydrometeor image is larger than 16 pixels, a circularity parameter is calculated to
24 distinguish non-spherical ice crystals (with circularity larger than 1.25) from spherical
25 liquid droplets (Crosier et al., 2011). In our two case studies, almost all the
26 hydrometeors with size larger than 250 μm were identified as ice crystals. Ice water
27 contents (IWC) are then derived from the hydrometeor PSD using two power law
28 mass-diameter (m-D) relationships: the modified Brown and Francis (1995) and
29 Leinonen and Szyrmer (2015). In both relationships, the maximum dimension ($D =$
30 D_{max}) is used and we assume that all hydrometeors with size larger than 75 μm are
31 ice crystals. The measurement uncertainty on the crystal dimension is typically around
32 20% while it reaches at least 50% for the number concentration, N_{ice} , (Baumgardner
33 et al., 2017; McFarquhar et al., 2017; Gurganus and Lawson, 2018). In the MPC
34 layers dominated by ice crystals, a systematic uncertainty of 50% can be assumed
35 for the IWC according to Heymsfield et al. (2010) and Hogan et al. (2012). Moreover,
36 the estimated statistical uncertainty in the PSD is typically a few percent but maxima
37 close to 70% are reached for number concentration below 10^{-5} cm^{-3} . CIP particle size
38 distributions are published in Dupuy et al. (2019);
- 39
40 vi. *Condensation Particle Counter (CPC TSI-3010) (Polar 6)* provides the total aerosol
41 particle number concentration in the diameter range 10 nm to 3 μm using light
42 scattering technique to detect and count aerosol grown by condensation inside the
43 instrument (Mertes et al., 1995). The CPC was connected behind a counterflow virtual
44 impactor (CVI, Twohy et al., 2003) inlet. Inside clouds, the CVI counterflow was
45 switched on (with a cut-off diameter around 10 μm) allowing the CPC to measure the
46 number concentration of the cloud droplet residuals which are representative of the
47 cloud condensation nuclei (CCN). In clear sky conditions, the counterflow was
48 switched off and the ambient aerosol number concentration can be measured by the
49 CPC. Details on the CVI operation, its characteristics (cut-off diameter, enrichment
50 factor, counterflow) and the CPC data are published in Mertes et al. (2019) and Ehrlich
51 et al. (2019).

1
2 vii. Ultra-High Sensitivity Aerosol Spectrometers (UHSAS-1 and UHSAS-2) (Polar 6)
3 measure the aerosol particle number size distribution for optical diameters ranging
4 from 60 or 80 to 1000 nm (with a 2 to 30 nm resolution) based on the intensity of the
5 laser light scattered by the particles (Cai et al., 2008). The UHSAS-1 was plugged to
6 the CVI inlet while the UHSAS-2 was alternatively connected to the total aerosol inlet
7 (stainless-steel inlet with shrouded diffuser) or the CVI inlet. These instruments are
8 used in our study to estimate and inter-compare CCN and total aerosol concentrations
9 with the ones measured by the CPC. UHSAS-2 Aerosol size distributions are also
10 exploited to derive ice nuclei particle (INP) number concentrations based on the
11 parameterisation of DeMott et al. (2010) which relates the INP concentration to the air
12 temperature T and the number concentration of the aerosol particles with diameters
13 larger than 500 nm. More details on the UHSAS-2 settings, measurements and data
14 processing as well as on the aerosol inlets are available in Zanatta et al. (2023).
15 UHSAS-1 and UHSAS-2 data are published respectively, in Mertes et al. (2019) and
16 Zanatta and Herber (2019).
17

18 **Data availability**

19 The datasets analysed for this study can be found in the PANGAEA (Data Publisher for Earth
20 and Environmental Science) database: <https://www.pangaea.de/?t=Atmosphere>. In addition,
21 the datasets can be accessed by using the ac3airborne python package (Mech et al., 2022).
22 All the datasets are listed in the references section.
23

24 **Author contributions**

25 D.A. performed the simulations and the data analysis and prepared a first version of the
26 manuscript with the help of C.P., O.J. and W.W.. S.B. installed the WRF model and the CR-
27 SIM module on the national calculators. R.D., A.B., G.M., and O.J. contributed to the analyses
28 of the *in situ* aircraft data. C.P. and W.W. contributed to the analyses of the WRF simulations
29 and comparisons between observations and simulation results. J-L.B. contributed to the
30 analyses using the CAT model. F.T. contributed to the analyses of the radar observations.
31 M.M. processed and helped analysing the radar data, so did S.M. with the aerosol
32 measurements, and A.E. with the dropsonde data. M.W. and A.E. designed the ALOUD
33 campaign, M.W. and M.M. the specific flight plan of the analysed case study. C.P., O.J., and
34 W.W. supervised D.A. All the authors contributed to the final writing/reading of the manuscript.

35 **Funding**

36 The lead author was funded by a doctoral fellowship from the Ecole Doctorale des Sciences
37 Fondamentales (EDSF) of the University Clermont Auvergne (UCA). This work is a contribution
38 to the ACME and (MPC)² projects, supported by the Agence Nationale de la Recherche under
39 the Grants ANR-21-CE01-0003 and ANR-22-CE01-0009, respectively. The model calculations
40 have been done on the French computer GENCI facilities of the Institut du Développement
41 des ressources en Informatique Scientifique (IDRIS) CNRS at Orsay, the Centre Informatique
42 National de l'Enseignement Supérieur (CINES) at Montpellier, the Très Grand Centre de
43 Calcul (TGCC) at the CEA, under the project 05056 and the Centre Régional de Ressources
44 Informatiques (CRR) UCA at Clermont-Ferrand. We gratefully acknowledge the funding by
45 the Deutsche Forschungsgemeinschaft (DFG, German Research Foundation) – Project
46 Number 268020496 – TRR 172, within the Transregional Collaborative Research Center
47 “Arctic Amplification: Climate Relevant Atmospheric and Surface Processes, and Feedback
48 Mechanisms (AC)³”.

1 **Conflict of interest**

2 The authors declare no conflict of interest.

3 **Acknowledgements**

4 The authors acknowledge all the persons involved in the ACLOUD campaign for collecting and
5 supplying the data used in this study. D.A. would also like to acknowledge Johannes Stapf for
6 the details he provided about the radiative data, which are available via the PANGAEA
7 database. S.B. would like to thank the members of the CR-SIM team for their help in installing
8 this module.

9 **References**

- 10 Achtert, P., O'Connor, E.J., Brooks, I.M., Sotiropoulou, G., Shupe, M.D., Pospichal, B., Brooks, B.J.,
11 Tjernström, M., 2020. Properties of Arctic liquid and mixed-phase clouds from shipborne Cloudnet
12 observations during ACSE 2014. *Atmospheric Chemistry and Physics* 20, 14983–15002.
13 <https://doi.org/10.5194/acp-20-14983-2020>
14
- 15 Arteaga, D., 2023. Étude des nuages arctiques en phase mixte observés en juin 2017 lors de la
16 campagne ACLOUD à l'aide du modèle atmosphérique WRF. Ph.D. Thesis, Université Clermont
17 Auvergne, Clermont-Ferrand, France. <https://theses.hal.science/tel-04457232>
18
- 19 Avramov, A., Ackerman, A.S., Fridlind, A.M., van Diedenhoven, B., Botta, G., Aydin, K., Verlinde, J.,
20 Korolev, A.V., Strapp, J.W., McFarquhar, G.M., Jackson, R., Brooks, S.D., Glen, A., Wolde, M., 2011.
21 Toward ice formation closure in Arctic mixed-phase boundary layer clouds during ISDAC. *Journal of*
22 *Geophysical Research: Atmospheres* 116. <https://doi.org/10.1029/2011JD015910>
23
- 24 Baray, J.-L., Deguillaume, L., Colomb, A., Sellegri, K., Freney, E., Rose, C., et al., 2020. Cézeaux-
25 Aulnat-Opme-Puy De Dôme: A multi-site for the long-term survey of the tropospheric composition and
26 climate change. *Atmos. Meas. Tech.* 13, 3413–3445. <https://doi.org/10.5194/amt-13-3413-2020>.
27
- 28 Baudoux, A., 2022. Impact des conditions environnementales sur les propriétés microphysiques des
29 nuages en Arctique. Master's thesis, Université Clermont Auvergne, Clermont Ferrand, France.
30
- 31 Baumgardner, D., Avallone, L., Bansemer, A., Borrmann, S., Brown, P., Bundke, U., Chuang, P.Y.,
32 Cziczo, D., Field, P., Gallagher, M., Gayet, J.-F., Heymsfield, A., Korolev, A., Krämer, M., McFarquhar,
33 G., Mertes, S., Möhler, O., Lance, S., Lawson, P., Petters, M.D., Pratt, K., Roberts, G., Rogers, D.,
34 Stetzer, O., Stith, J., Strapp, W., Twohy, C., Wendisch, M., 2012. In Situ, Airborne Instrumentation:
35 Addressing and Solving Measurement Problems in Ice Clouds. *Bulletin of the American Meteorological*
36 *Society* 93, ES29–ES34. <https://doi.org/10.1175/BAMS-D-11-00123.1>.
37
- 38 Baumgardner, D., Brenguier, J., Bucholtz, A., Coe, H., DeMott, P., Garrett, T., et al., 2011. Airborne
39 instruments to measure atmospheric aerosol particles, clouds and radiation: A cook's tour of mature and
40 emerging technology. *Atmos. Res.* 102, 10–29. <https://doi.org/10.1016/j.atmosres.2011.06.021>.
41
- 42 Baumgardner, D., Jonsson, H., Dawson, W., O'Connor, D., and Newton, R., 2017. The cloud, aerosol
43 and precipitation spectrometer: a new instrument for cloud investigations. *Atmos. Res.* 59, 251–264.
44 [https://doi.org/10.1016/S0169-8095\(01\)00119-3](https://doi.org/10.1016/S0169-8095(01)00119-3).
45
- 46 Becker, S., Ehrlich, A., Schäfer, M., Wendisch, M., 2023. Airborne observations of the surface cloud
47 radiative effect during different seasons over sea ice and open ocean in the Fram Strait. *Atmospheric*
48 *Chemistry and Physics* 23, 7015–7031. <https://doi.org/10.5194/acp-23-7015-2023>
49
- 50 Bezdek, A., and Sebera, J., 2013. MATLAB script for 3D visualizing geodata on a rotating globe,
51 *Comput. Geosci.* 56, 127–130, <https://doi.org/10.1016/j.cageo.2013.03.007>, 2013.
52

1 Boisvert, L.N., Wu, D.L., Vihma, T., Susskind, J., 2015. Verification of air/surface humidity differences
2 from AIRS and ERA-Interim in support of turbulent flux estimation in the Arctic. *Journal of Geophysical*
3 *Research: Atmospheres* 120, 945–963. <https://doi.org/10.1002/2014JD021666>
4
5 Bromwich, D. H., Hines, K. M., and Bai, L.-S., 2009. Development and testing of Polar Weather
6 Research and Forecasting model: 2. Arctic Ocean. *J. Geophys. Res.-Atmos.* 114, D08122.
7 <https://doi.org/10.1029/2008JD010300>.
8
9 Brown, P. R. A. and Francis, P. N., 1995. Improved measurements of the ice water content in cirrus
10 using a total-water probe. *J. Atmos. Ocean. Tech.* 12, 410–414. [https://doi.org/10.1175/1520-](https://doi.org/10.1175/1520-0426(1995)0122.0.CO;2)
11 [0426\(1995\)0122.0.CO;2](https://doi.org/10.1175/1520-0426(1995)0122.0.CO;2).
12
13 Cai, Y., D.C. Montague, W. Mooiweer-Bryan, T. Deshler, 2008. Performance characteristics of the ultra
14 high sensitivity aerosol spectrometer for particles between 55 and 800 nm: Laboratory and field studies.
15 *Journal of Aerosol Science.* 39, 759-769. <https://doi.org/10.1016/j.jaerosci.2008.04.007>.
16
17 Chechin, D.G., Lüpkes, C., Hartmann, J., Ehrlich, A., Wendisch, M., 2023. Turbulent structure of the
18 Arctic boundary layer in early summer driven by stability, wind shear and cloud-top radiative cooling:
19 ACLOUD airborne observations. *Atmospheric Chemistry and Physics* 23, 4685–4707.
20 <https://doi.org/10.5194/acp-23-4685-2023>
21
22 Chen, F. and Dudhia, J., 2001. Coupling an Advanced Land Surface-Hydrology Model with the Penn
23 State-NCAR MM5 Modeling System. Part I: Model Implementation and Sensitivity. *Mon. Wea. Rev.* 129,
24 569–585. [https://doi.org/10.1175/1520-0493\(2001\)129<0569:CAALSH>2.0.CO;2](https://doi.org/10.1175/1520-0493(2001)129<0569:CAALSH>2.0.CO;2).
25
26 Cho, H., Jun, S.-Y., Ho, C.-H., McFarquhar, G., 2020. Simulations of winter Arctic clouds and associated
27 radiation fluxes using different cloud microphysics schemes in the Polar WRF: Comparisons with
28 CloudSat, CALIPSO, and CERES. *Journal of Geophysical Research: Atmospheres*, 125,
29 e2019JD031413. <https://doi.org/10.1029/2019JD031413>
30
31 Chylik, J., Chechin, D., Dupuy, R., Kulla, B.S., Lüpkes, C., Mertes, S., Mech, M., Neggers, R.A.J., 2023.
32 Aerosol impacts on the entrainment efficiency of Arctic mixed-phase convection in a simulated air mass
33 over open water. *Atmos. Chem. Phys.* 23, 4903–4929. <https://doi.org/10.5194/acp-23-4903-2023>
34
35 Copernicus Climate Change Service (C3S), 2017. ERA5: Fifth Generation of ECMWF Atmospheric
36 Reanalyses of the Global Climate (Copernicus Climate Change Service Climate Data Store (CDS)).
37
38 Coopman, Q., Riedi, J., Finch, D.P., Garrett, T.J., 2018. Evidence for Changes in Arctic Cloud Phase
39 Due to Long-Range Pollution Transport. *Geophysical Research Letters* 45, 10,709-10,718.
40 <https://doi.org/10.1029/2018GL079873>
41
42 Crosier, J., Bower, K. N., Choularton, T. W., Westbrook, C. D., Connolly, P. J., Cui, Z. Q., et al., 2011.
43 Observations of ice multiplication in a weakly convective cell embedded in supercooled mid-level stratus.
44 *Atmos. Chem. Phys.* 11, 257–273. <https://doi.org/10.5194/acp-11-257-2011>.
45
46 Curry, J.A., Hobbs, P.V., King, M.D., Randall, D.A., Minnis, P., Isaac, G.A., Pinto, J.O., Uttal, T.,
47 Bucholtz, A., Cripe, D.G., Gerber, H., Fairall, C.W., Garrett, T.J., Hudson, J., Intrieri, J.M., Jakob, C.,
48 Jensen, T., Lawson, P., Marcotte, D., Nguyen, L., Pilewskie, P., Rangno, A., Rogers, D.C., Strawbridge,
49 K.B., Valero, F.P.J., Williams, A.G., Wylie, D., 2000. FIRE Arctic Clouds Experiment. *Bulletin of the*
50 *American Meteorological Society* 81, 5–30. [https://doi.org/10.1175/1520-](https://doi.org/10.1175/1520-0477(2000)081<0005:FACE>2.3.CO;2)
51 [0477\(2000\)081<0005:FACE>2.3.CO;2](https://doi.org/10.1175/1520-0477(2000)081<0005:FACE>2.3.CO;2).
52
53 de Boer, G., Hashino, T., Tripoli, G.J., 2010. Ice nucleation through immersion freezing in mixed-phase
54 stratiform clouds: Theory and numerical simulations. *Atmospheric Research*, 15th International
55 Conference on Clouds and Precipitation 96, 315–324. <https://doi.org/10.1016/j.atmosres.2009.09.012>
56

1 de Boer, G., Morrison, H., Shupe, M.D., Hildner, R., 2011. Evidence of liquid dependent ice nucleation
2 in high-latitude stratiform clouds from surface remote sensors. *Geophysical Research Letters* 38.
3 <https://doi.org/10.1029/2010GL046016>
4
5 de Lozar, A., Muessle, L., 2016. Long-resident droplets at the stratocumulus top. *Atmospheric Chemistry
6 and Physics* 16, 6563–6576. <https://doi.org/10.5194/acp-16-6563-2016>.
7
8 DeMott, P., Prenni, A., Liu, X., Kreidenweis, S., Petters, M., Twohy, C., et al., 2010. Predicting global
9 atmospheric ice nuclei distributions and their impacts on climate. *Proc. Natl. Acad. Sci.* 107, 11217–
10 11222. <https://doi.org/10.1073/pnas.0910818107>.
11
12 Dufour, A., Zolina, O., and Gulev, S. K., 2016. Atmospheric Moisture Transport to the Arctic: Assessment
13 of Reanalyses and Analysis of Transport Components. *J. Climate.* 29, 5061–5081.
14 <https://doi.org/10.1175/JCLI-D-15-0559.1>.
15
16 Dupuy, R., Jourdan, O., Mioche, G., Ehrlich, A., Waitz, F., Gourbeyre, C., et al., 2018. Cloud
17 microphysical properties of summertime Arctic stratocumulus during the ACLOUD campaign:
18 Comparison with previous results in the European Arctic. In 15th Conference on Cloud Physics
19 (Vancouver, Canada), <http://hal.archives-ouvertes.fr/hal-01932907>.
20
21 [Dataset] Dupuy, R., Jourdan, O., Mioche, G., Gourbeyre, C., Leroy, D., and Schwarzenböck, A., 2019.
22 CDP, CIP and PIP: In-situ Arctic cloud microphysical properties observed during ACLOUD-AC3
23 campaign in June 2017. <https://doi.org/10.1594/PANGAEA.899074>.
24
25 Egerer, U., Ehrlich, A., Gottschalk, M., Griesche, H., Neggers, R. A. J., Siebert, H., and Wendisch, M.,
26 2021. Case study of a humidity layer above Arctic stratocumulus and potential turbulent coupling with
27 the cloud top, *Atmos. Chem. Phys.*, 21, 6347–6364, <https://doi.org/10.5194/acp-21-6347-2021>
28
29 Ehrlich, A., Wendisch, M., Bierwirth, E., Gayet, J.-F., Mioche, G., Lampert, A., et al., 2009. Evidence of
30 ice crystals at cloud top of Arctic boundary-layer mixed-phase clouds derived from airborne remote
31 sensing. *Atmos. Chem. Phys.* 9, 9401–9416. <https://doi.org/10.5194/acp-9-9401-2009>.
32
33 Ehrlich, A., Wendisch, M., Lüpkes, C., Buschmann, M., Bozem, H., Chechin, D., et al., 2019a. A
34 comprehensive in situ and remote sensing data set from the Arctic CLOUD Observations Using airborne
35 measurements during polar Day (ACLOUD) campaign. *Earth System Science Data.* 11, 1853–1881.
36 <https://doi.org/10.5194/essd-11-1853-2019>.
37
38 [Dataset] Ehrlich, A., Wendisch, M., Lüpkes, C., Buschmann, M., Bozem, H., Chechin, D., et al., 2019b.
39 Collection of data sources for the Arctic CLOUD Observations Using airborne measurements during polar
40 Day (ACLOUD) campaign, North-West of Svalbard between 23 May - 26 June 2017.
41 <https://doi.org/10.1594/PANGAEA.902603>.
42
43 Eirund, G., Possner, A., and Lohmann, U., 2019. Response of Arctic mixed-phase clouds to aerosol
44 perturbations under different surface forcings. *Atmos. Chem. Phys.* 19, 9847–9864.
45 <https://doi.org/10.5194/acp-19-9847-2019>.
46
47 Fan, J., Wang, Y., Rosenfeld, D., Liu, X., 2016. Review of Aerosol–Cloud Interactions: Mechanisms,
48 Significance, and Challenges. *Journal of the Atmospheric Sciences* 73, 4221–4252.
49 <https://doi.org/10.1175/JAS-D-16-0037.1>
50
51 Field, P.R., Lawson, R.P., Brown, P.R.A., Lloyd, G., Westbrook, C., Moisseev, D., Miltenberger, A.,
52 Nenes, A., Blyth, A., Choularton, T., Connolly, P., Buehl, J., Crosier, J., Cui, Z., Dearden, C., DeMott,
53 P., Flossmann, A., Heymsfield, A., Huang, Y., Kalesse, H., Kanji, Z.A., Korolev, A., Kirchgassner, A.,
54 Lasher-Trapp, S., Leisner, T., McFarquhar, G., Phillips, V., Stith, J., Sullivan, S., 2017. Secondary Ice
55 Production: Current State of the Science and Recommendations for the Future. *Meteorological
56 Monographs* 58, 7.1-7.20. <https://doi.org/10.1175/AMSMONOGRAPHS-D-16-0014.1>

1
2 Flossmann, A. I., and Wobrock, W., 2010. A review of our understanding of the aerosol-cloud interaction
3 from the perspective of a bin resolved cloud scale modelling. *Atmos. Res.* 97(4), 2010, 478–497.
4 <https://doi.org/10.1016/j.atmosres.2010.05.008>.
5
6 Fridlind, A.M., Ackerman, A.S., 2018. Chapter 7 - Simulations of Arctic Mixed-Phase Boundary Layer
7 Clouds: Advances in Understanding and Outstanding Questions, in: Andronache, C. (Ed.), *Mixed-Phase*
8 *Clouds*. Elsevier, pp. 153–183. <https://doi.org/10.1016/B978-0-12-810549-8.00007-6>
9
10 Fridlind, A.M., Ackerman, A.S., McFarquhar, G., Zhang, G., Poellot, M.R., DeMott, P.J., Prenni, A.J.,
11 Heymsfield, A.J., 2007. Ice properties of single-layer stratocumulus during the Mixed-Phase Arctic Cloud
12 Experiment: 2. Model results. *Journal of Geophysical Research: Atmospheres* 112.
13 <https://doi.org/10.1029/2007JD008646>
14
15 Gayet, J.-F., Mioche, G., Dörnbrack, A., Ehrlich, A., Lampert, A., Wendisch, M., 2009. Microphysical
16 and optical properties of Arctic mixed-phase clouds. The 9 April 2007 case study. *Atmospheric*
17 *Chemistry and Physics* 9, 6581–6595. <https://doi.org/10.5194/acp-9-6581-2009>
18
19 Gierens, R., Kneifel, S., Shupe, M. D., Ebell, K., Maturilli, M., and Löhnert, U., 2020. Low-level mixed-
20 phase clouds in a complex Arctic environment. *Atmos. Chem. Phys.* 20, 3459–3481.
21 <https://doi.org/10.5194/acp-20-3459-2020>.
22
23 Griesche, H. J., Ohneiser, K., Seifert, P., Radenz, M., Engelmann, R., and Ansmann, A., 2021.
24 Contrasting ice formation in Arctic clouds: surface-coupled vs. surface-decoupled clouds. *Atmos. Chem.*
25 *Phys.* 21, 10357–10374. <https://doi.org/10.5194/acp-21-10357-2021>.
26
27 Gultepe, I., Isaac, G., Hudak, D., Nissen, R., and Strapp, J. W., 2000. Dynamical and Microphysical
28 Characteristics of Arctic Clouds during BASE. *J. Climate.* 13, 1225–1254. [https://doi.org/10.1175/1520-](https://doi.org/10.1175/1520-0442(2000)0132.0.CO;2)
29 [0442\(2000\) 0132.0.CO;2](https://doi.org/10.1175/1520-0442(2000)0132.0.CO;2).
30
31 Gultepe, I. and Isaac, G. A., 2002. Effects of air mass origin on Arctic cloud microphysical parameters
32 for April 1998 during FIRE.ACE. *J. Geophys. Res.-Atmos.* 107(C10).
33 <https://doi.org/10.1029/2000JC000440>.
34
35 Gurganus, C., and Lawson, P., 2018. Laboratory and Flight Tests of 2D Imaging Probes: Toward a
36 Better Understanding of Instrument Performance and the Impact on Archived Data, *J. Atmos. Ocean.*
37 *Tech.*, 35, 1533–1553, <https://doi.org/10.1175/jtech-d-17-0202.1>.
38
39 Harrington, J.Y., Reisin, T., Cotton, W.R., Kreidenweis, S.M., 1999. Cloud resolving simulations of Arctic
40 stratus: Part II: Transition-season clouds. *Atmospheric Research* 51, 45–75.
41 [https://doi.org/10.1016/S0169-8095\(98\)00098-2](https://doi.org/10.1016/S0169-8095(98)00098-2)
42
43 Hartmann, M., Gong, X., Kecorius, S., van Pinxteren, M., Vogl, T., Welti, A., Wex, H., Zeppenfeld, S.,
44 Herrmann, H., Wiedensohler, A., Stratmann, F., 2021. Terrestrial or marine – indications towards the
45 origin of ice-nucleating particles during melt season in the European Arctic up to 83.7°N. *Atmospheric*
46 *Chemistry and Physics* 21, 11613–11636. <https://doi.org/10.5194/acp-21-11613-2021>
47
48 Hersbach, H., Bell, B., Berrisford, P., Biavati, G., Horányi, A., Muñoz Sabater, J., Nicolas, J., Peubey,
49 C., Radu, R., Rozum, I., Schepers, D., Simmons, A., Soci, C., Dee, D., Thépaut, J.-N., 2023a. ERA5
50 hourly data on single levels from 1940 to present. Copernicus Climate Change Service (C3S) Climate
51 Data Store (CDS), DOI: 10.24381/cds.adbb2d47
52
53 Hersbach, H., Bell, B., Berrisford, P., Biavati, G., Horányi, A., Muñoz Sabater, J., Nicolas, J., Peubey,
54 C., Radu, R., Rozum, I., Schepers, D., Simmons, A., Soci, C., Dee, D., Thépaut, J.-N., 2023b. ERA5
55 hourly data on pressure levels from 1940 to present. Copernicus Climate Change Service (C3S) Climate
56 Data Store (CDS), DOI: 10.24381/cds.bd0915c6

1
2 Heymsfield, A. J., Schmitt, C., Bansemer, A., and Twohy, C. H., 2010. Improved Representation of Ice
3 Particle Masses Based on Observations in Natural Clouds, *J. Atmos. Sci.*, 67, 3303–3318,
4 <https://doi.org/10.1175/2010jas3507.1>.
5
6 Hines, K. M. and Bromwich, D. H., 2008. Development and testing of Polar WRF. Part I: Greenland Ice
7 Sheet meteorology. *Mon. Wea. Rev.* 136, 1971–1989. <https://doi.org/10.1175/2007MWR2112.1>.
8
9 Hines, K. M., and D. H. Bromwich, 2017. Simulation of Late Summer Arctic Clouds during ASCOS with
10 Polar WRF. *Mon. Wea. Rev.*, 145, 521–541, <https://doi.org/10.1175/MWR-D-16-0079.1>.
11
12 Hines, K. M., Bromwich, D. H., Bai, L.-S., Barlage, M., and Slater, A. G., 2011. Development and Testing
13 of Polar WRF. Part III: Arctic Land. *J. Climate*. 24, 26–48. <https://doi.org/10.1175/2010JCLI3460.1>.
14
15 Hogan, R. J., Tian, L., Brown, P. R. A., Westbrook, C. D., Heymsfield, A. J., and Eastment, J. D., 2012.
16 Radar Scattering from Ice Aggregates Using the Horizontally Aligned Oblate Spheroid Approximation,
17 *J. Appl. Meteorol. Clim.*, 51, 655–671, <https://doi.org/10.1175/jamc-d-11-074.1>.
18
19 Hogan, R.J., Honeyager, R., Tyynelä, J. and Kneifel, S., 2017. Calculating the millimetre-wave scattering
20 phase function of snowflakes using the self-similar Rayleigh–Gans Approximation. *Q.J.R. Meteorol.*
21 *Soc.*, 143: 834-844. <https://doi.org/10.1002/qj.2968>
22
23 Hong, S., and Lim, J.J., 2006. The WRF Single-Moment 6-Class Microphysics Scheme (WSM6). *Asia-*
24 *pacific Journal of Atmospheric Sciences*, 42, 129-151.
25
26 Iacono, M., Delamere, J., Mlawer, E. J., Shephard, M., Clough, S., and Collins, W. D., 2008. Radiative
27 forcing by long-lived greenhouse gases: Calculations with the AER radiative transfer models. *J.*
28 *Geophys. Res.-Atmos.* 113, D13103. <https://doi.org/10.1029/2008JD009944>.
29
30 Iacono, M. J., 2011. Application of Improved Radiation Modeling to General Circulation Models
31 (Atmospheric and Environmental Research, Inc.), Final Technical Report Edn.
32
33 Ikonen, I., Demetriades, N. W. S., and Holle, R., 2010. Vaisala dropsondes: History, status, and
34 applications. In 29th Conference on Hurricanes and Tropical Meteorology (SPONSOR, Tucson, Ariz.),
35 1–4.
36
37 Irish, V.E., Hanna, S.J., Willis, M.D., China, S., Thomas, J.L., Wentzell, J.J.B., Cirisan, A., Si, M., Leaitch,
38 W.R., Murphy, J.G., Abbatt, J.P.D., Laskin, A., Girard, E., Bertram, A.K., 2019. Ice nucleating particles
39 in the marine boundary layer in the Canadian Arctic during summer 2014. *Atmospheric Chemistry and*
40 *Physics* 19, 1027–1039. <https://doi.org/10.5194/acp-19-1027-2019>
41
42 Jackson, R.C., McFarquhar, G.M., Korolev, A.V., Earle, M.E., Liu, P.S.K., Lawson, R.P., Brooks, S.,
43 Wolde, M., Laskin, A., Freer, M., 2012. The dependence of ice microphysics on aerosol concentration
44 in Arctic mixed-phase stratus clouds during ISDAC and M-PACE. *Journal of Geophysical Research:*
45 *Atmospheres* 117. <https://doi.org/10.1029/2012JD017668>
46
47 Janjic, Z., 2002. Nonsingular Implementation of the Mellor-Yamada Level 2.5 Scheme in the NCEP
48 Meso Model. NCEP Office Note 437, 61.
49
50 Järvinen, E., Nehlert, F., Xu, G., Waitz, F., Mioche, G., Dupuy, R., Jourdan, O., and Schnaiter, M., 2023.
51 Investigating the vertical extent and short-wave radiative effects of the ice phase in Arctic summertime
52 low-level clouds. *Atmos. Chem. Phys.* 23, 7611–7633. <https://doi.org/10.5194/acp-23-7611-2023>.
53
54 Jensen, A. A., Harrington, J. Y., Morrison, H., and Milbrandt, J. A. 2017. Predicting Ice Shape Evolution
55 in a Bulk Microphysics Model. *J. Atmos. Sci.*, 74, 2081–2104, <https://doi.org/10.1175/JAS-D-16-0350.1>.
56

1 Jourdan, O., Mioche, G., Garrett, T.J., Schwarzenböck, A., Vidot, J., Xie, Y., Shcherbakov, V., Yang, P.,
2 Gayet, J.-F., 2010. Coupling of the microphysical and optical properties of an Arctic nimbostratus cloud
3 during the ASTAR 2004 experiment: Implications for light-scattering modeling. *J. Geophys. Res.* 115,
4 D23206. <https://doi.org/10.1029/2010JD014016>
5
6 Karalis, M., Sotiropoulou, G., Abel, S.J., Bossioli, E., Georgakaki, P., Methymaki, G., Nenes, A.,
7 Tombrou, M., 2022. Effects of secondary ice processes on a stratocumulus to cumulus transition during
8 a cold-air outbreak. *Atmospheric Research* 277, 106302.
9 <https://doi.org/10.1016/j.atmosres.2022.106302>
10
11 Kay, J.E., Holland, M.M., Bitz, C.M., Blanchard-Wrigglesworth, E., Gettelman, A., Conley, A., Bailey, D.,
12 2012. The Influence of Local Feedbacks and Northward Heat Transport on the Equilibrium Arctic Climate
13 Response to Increased Greenhouse Gas Forcing. *Journal of Climate* 25, 5433–5450.
14 <https://doi.org/10.1175/JCLI-D-11-00622.1>
15
16 Keita, S.A., Girard, E., Raut, J.-C., Leriche, M., Blanchet, J.-P., Pelon, J., Onishi, T., Cirisan, A., 2020.
17 A new parameterization of ice heterogeneous nucleation coupled to aerosol chemistry in WRF-Chem
18 model version 3.5.1: evaluation through ISDAC measurements. *Geosci. Model Dev.* 13, 5737–5755.
19 <https://doi.org/10.5194/gmd-13-5737-2020>
20
21 Khairoutdinov, M., and Y. Kogan, 2000. A New Cloud Physics Parameterization in a Large-Eddy
22 Simulation Model of Marine Stratocumulus. *Mon. Wea. Rev.* 128, 229–243.
23 [https://doi.org/10.1175/1520-0493\(2000\)128<0229:ANCPPI>2.0.CO;2](https://doi.org/10.1175/1520-0493(2000)128<0229:ANCPPI>2.0.CO;2)
24
25 Klein, S.A., McCoy, R.B., Morrison, H., Ackerman, A.S., Avramov, A., Boer, G. de, Chen, M., Cole,
26 J.N.S., Del Genio, A.D., Falk, M., Foster, M.J., Fridlind, A., Golaž, J.-C., Hashino, T., Harrington, J.Y.,
27 Hoose, C., Khairoutdinov, M.F., Larson, V.E., Liu, X., Luo, Y., McFarquhar, G.M., Menon, S., Neggers,
28 R.A.J., Park, S., Poellot, M.R., Schmidt, J.M., Sednev, I., Shipway, B.J., Shupe, M.D., Spangenberg,
29 D.A., Sud, Y.C., Turner, D.D., Veron, D.E., Salzen, K. von, Walker, G.K., Wang, Z., Wolf, A.B., Xie, S.,
30 Xu, K.-M., Yang, F., Zhang, G., 2009. Intercomparison of model simulations of mixed-phase clouds
31 observed during the ARM Mixed-Phase Arctic Cloud Experiment. I: single-layer cloud. *Quarterly Journal*
32 *of the Royal Meteorological Society* 135, 979–1002. <https://doi.org/10.1002/qj.416>
33
34 [Dataset] Kliesch, L.-L. and Mech, M., 2019. Airborne radar reflectivity and brightness temperature
35 measurements with POLAR 5 during ALOUD in May and June 2017.
36 <https://doi.org/10.1594/PANGAEA.899565>
37
38 Klingebiel, M., de Lozar, A., Molleker, S., Weigel, R., Roth, A., Schmidt, L., Meyer, J., Ehrlich, A.,
39 Neuber, R., Wendisch, M., Borrmann, S., 2015. Arctic low-level boundary layer clouds: in situ
40 measurements and simulations of mono- and bimodal supercooled droplet size distributions at the top
41 layer of liquid phase clouds. *Atmospheric Chemistry and Physics* 15, 617–631.
42 <https://doi.org/10.5194/acp-15-617-2015>
43
44 Klingebiel, M., Ehrlich, A., Ruiz-Donoso, E., Risse, N., Schirmacher, I., Jäkel, E., Schäfer, M., Wolf, K.,
45 Mech, M., Moser, M., Voigt, C., Wendisch, M., 2023. Variability and properties of liquid-dominated
46 clouds over the ice-free and sea-ice-covered Arctic Ocean. *Atmospheric Chemistry and Physics*
47 *Discussions* 1–24. <https://doi.org/10.5194/acp-2022-848>
48
49 Kneifel, S., Leinonen, J., Tyynelä, J., Ori, D., Battaglia, A., 2020. Scattering of Hydrometeors. In:
50 Levizzani, V., Kidd, C., Kirschbaum, D.B., Kummerow, C.D., Nakamura, K., Turk, F.J. (eds) *Satellite*
51 *Precipitation Measurement. Advances in Global Change Research*, vol 67. Springer, Cham.
52 https://doi.org/10.1007/978-3-030-24568-9_15
53
54 Knudsen, E. M., Heinold, B., Dahlke, S., Bozem, H., Crewell, S., Gorodetskaya, I. V., et al., 2018.
55 Meteorological conditions during the ALOUD/PASCAL field campaign near Svalbard in early summer
56 2017. *Atmos. Chem. Phys.* 18, 17995–18022. <https://doi.org/10.5194/acp-18-17995-2018>

1
2 Korolev, A., Isaac, G.A., 2006. Relative Humidity in Liquid, Mixed-Phase, and Ice Clouds. *Journal of the*
3 *Atmospheric Sciences* 63, 2865–2880. <https://doi.org/10.1175/JAS3784.1>
4
5 Korolev, A.V., Isaac, G.A., Cober, S.G., Strapp, J.W., Hallett, J., 2003. Microphysical characterization
6 of mixed-phase clouds. *Quarterly Journal of the Royal Meteorological Society* 129, 39–65.
7 <https://doi.org/10.1256/qj.01.204>
8
9 Korolev, A.V., Isaac, G.A., Strapp, J.W., Nevzorov, A.N., 1999. In situ measurements of effective
10 diameter and effective droplet number concentration. *J. Geophys. Res.* 104, 3993–4003.
11 <https://doi.org/10.1029/1998JD200071>
12
13 Korolev, A. and Leisner, T., 2020. Review of experimental studies of secondary ice production. *Atmos.*
14 *Chem. Phys.* 20, 11767–11797. <https://doi.org/10.5194/acp-20-11767-2020>.
15
16 Korolev, A., McFarquhar, G., Field, P.R., Franklin, C., Lawson, P., Wang, Z., Williams, E., Abel, S.J.,
17 Axisa, D., Borrmann, S., Crosier, J., Fugal, J., Krämer, M., Lohmann, U., Schlenczek, O., Schnaiter, M.,
18 Wendisch, M., 2017. Mixed-Phase Clouds: Progress and Challenges. *Meteorological Monographs* 58,
19 5.1-5.50. <https://doi.org/10.1175/AMSMONOGRAPHS-D-17-0001.1>
20
21 Kretschmar, J., Stapf, J., Klocke, D., Wendisch, M., and Quaas, J., 2020. Employing airborne radiation
22 and cloud microphysics observations to improve cloud representation in ICON at kilometer-scale
23 resolution in the Arctic. *Atmos. Chem. Phys.*, 20, 13145–13165, [https://doi.org/10.5194/acp-20-13145-](https://doi.org/10.5194/acp-20-13145-2020)
24 [2020](https://doi.org/10.5194/acp-20-13145-2020)
25
26 Küchler, N., Kneifel, S., Löhnert, U., Kollias, P., Czekala, H., and Rose, T., 2017. A W-band radar-
27 radiometer system for accurate and continuous monitoring of clouds and precipitation. *J. Atmos. Ocean.*
28 *Tech.* 34, 2375–2392. <https://doi.org/10.1175/JTECHD-17-0019.1>.
29
30 Lance, S., Shupe, M.D., Feingold, G., Brock, C.A., Cozic, J., Holloway, J.S., Moore, R.H., Nenes, A.,
31 Schwarz, J.P., Spackman, J.R., Froyd, K.D., Murphy, D.M., Brioude, J., Cooper, O.R., Stohl, A.,
32 Burkhart, J.F., 2011. Cloud condensation nuclei as a modulator of ice processes in Arctic mixed-phase
33 clouds. *Atmos. Chem. Phys.* 11, 8003–8015. <https://doi.org/10.5194/acp-11-8003-2011>
34
35 Leck, C. and Svensson, E., 2015. Importance of aerosol composition and mixing state for cloud droplet
36 activation over the Arctic pack ice in summer. *Atmos. Chem. Phys.* 15, 2545–2568.
37 <https://doi.org/10.5194/acp-15-2545-2015>.
38
39 Leinonen, J. and Szyrmer, W., 2015. Radar signatures of snowflake riming: A modeling study. *Earth*
40 *and Space Science* 2, 346–358. <https://doi.org/10.1002/2015EA000102>.
41
42 Leroy, D., Fontaine, E., Schwarzenboeck, A., and Strapp, J. W., 2016. Ice Crystal Sizes in High Ice
43 Water Content Clouds. Part I: On the Computation of Median Mass Diameter from In Situ
44 Measurements. *J. Atmos. Ocean. Tech.* 33, 2461–2476. <https://doi.org/10.1175/JTECH-D-15-0151.1>.
45
46 Lloyd, G., Choulaton, T. W., Bower, K. N., Crosier, J., Jones, H., Dorsey, J. R., et al., 2015.
47 Observations and comparisons of cloud microphysical properties in spring and summertime Arctic
48 stratocumulus clouds during the ACCACIA campaign. *Atmos. Chem. Phys.* 15, 3719–3737.
49 <https://doi.org/10.5194/acp-15-3719-2015>.
50
51 Ludwig, V., Spreen, G., Haas, C., Istomina, L., Kauker, F., and Murashkin, D., 2019. The 2018 North
52 Greenland polynya observed by a newly introduced merged optical and passive microwave sea-ice
53 concentration dataset. *The Cryosphere.* 13, 2051–2073. <https://doi.org/10.5194/tc-13-2051-2019>.
54

1 Martin, G. M., Johnson, D. W., and Spice, A., 1994. The Measurement and Parameterization of Effective
2 Radius of Droplets in Warm Stratocumulus Clouds. *J. Atmos. Sci.* 51, 1823–1842.
3 [https://doi.org/10.1175/1520-0469\(1994\)051<1823:TMAPOE>2.0.CO;2](https://doi.org/10.1175/1520-0469(1994)051<1823:TMAPOE>2.0.CO;2).
4
5 Matus, A.V., L'Ecuyer, T.S., 2017. The role of cloud phase in Earth's radiation budget: CLOUD PHASE
6 IN EARTH'S RADIATION BUDGET. *J. Geophys. Res. Atmos.* 122, 2559–2578.
7 <https://doi.org/10.1002/2016JD025951>
8
9 McFarquhar, G.M., Ghan, S., Verlinde, J., Korolev, A., Strapp, J.W., Schmid, B., Tomlinson, J.M.,
10 Wolde, M., Brooks, S.D., Cziczo, D., Dubey, M.K., Fan, J., Flynn, C., Gultepe, I., Hubbe, J., Gilles, M.K.,
11 Laskin, A., Lawson, P., Leaitch, W.R., Liu, P., Liu, X., Lubin, D., Mazzoleni, C., Macdonald, A.-M., Moffet,
12 R.C., Morrison, H., Ovchinnikov, M., Shupe, M.D., Turner, D.D., Xie, S., Zelenyuk, A., Bae, K., Freer,
13 M., Glen, A., 2011. Indirect and Semi-direct Aerosol Campaign: The Impact of Arctic Aerosols on Clouds.
14 *Bull. Amer. Meteor. Soc.* 92, 183–201. <https://doi.org/10.1175/2010BAMS2935.1>
15
16 McFarquhar, G. M. and Heymsfield, A. J., 1996. Microphysical characteristics of three anvils sampled
17 during the Central Equatorial Pacific Experiment. *J. Atmos. Sci.* 53, 2401–2423.
18 [https://doi.org/10.1175/1520-0469\(1996\)053,2401:MCOTAS.2.0.CO;2](https://doi.org/10.1175/1520-0469(1996)053,2401:MCOTAS.2.0.CO;2).
19
20 McFarquhar, G.M., Zhang, G., Poellot, M.R., Kok, G.L., McCoy, R., Tooman, T., Fridlind, A., Heymsfield,
21 A.J., 2007. Ice properties of single-layer stratocumulus during the Mixed-Phase Arctic Cloud
22 Experiment: 1. Observations. *J. Geophys. Res.* 112, D24201. <https://doi.org/10.1029/2007JD008633>
23
24 McFarquhar, G. M., Baumgardner, D., Bansemer, A., Abel, S. J., Crosier, J., French, J., Rosenberg, P.,
25 Korolev, A., Schwarzenboeck, A., Leroy, D., Um, J., Wu, W., Heymsfield, A. J., Twohy, C., Detwiler, A.,
26 Field, P., Neumann, A., Cotton, R., Axisa, D., and Dong, J., 2017. Processing of Ice Cloud In Situ Data
27 Collected by Bulk Water, Scattering, and Imaging Probes: Fundamentals, Uncertainties, and Efforts
28 toward Consistency, *Meteorol. Monogr.*, 58, 11.1–11.33, <https://doi.org/10.1175/amsmonographs-d-16-0007.1>.
29
30
31 McIlhattan, E.A., Kay, J.E., L'Ecuyer, T.S., 2020. Arctic Clouds and Precipitation in the Community Earth
32 System Model Version 2. *Journal of Geophysical Research: Atmospheres* 125, e2020JD032521.
33 <https://doi.org/10.1029/2020JD032521>
34
35 Mech, M., Ehrlich, A., Herber, A., Lüpkes, C., Wendisch, M., Becker, S., Boose, Y., Chechin, D., Crewell,
36 S., Dupuy, R., Gourbeyre, C., Hartmann, J., Jäkel, E., Jourdan, O., Kliesch, L.-L., Klingebiel, M., Kulla,
37 B.S., Mioche, G., Moser, M., Risse, N., Ruiz-Donoso, E., Schäfer, M., Stapf, J., Voigt, C., 2022.
38 MOSAiC-ACA and AFLUX - Arctic airborne campaigns characterizing the exit area of MOSAiC. *Sci Data*
39 9, 790. <https://doi.org/10.1038/s41597-022-01900-7>
40
41 Mech, M., Kliesch, L.-L., Anhäuser, A., Rose, T., Kollias, P., and Crewell, S., 2019. Microwave
42 Radar/radiometer for Arctic Clouds (MiRAC): first insights from the ALOUD campaign. *Atmos. Meas.*
43 *Tech.* 12, 5019–5037. <https://doi.org/10.5194/amt-12-5019-2019>.
44
45 Mertes, S., Schröder, F., and Wiedensohler, A., 1995. The particle detection efficiency curve of the Tsi-
46 3010 CPC as a function of the temperature difference between saturator and condenser. *Aerosol. Sci.*
47 *Technol.* 23, 257–261. <https://doi.org/10.1080/02786829508965310>.
48
49 [Dataset] Mertes, S., Kästner, U., and Macke, A., 2019. Airborne in-situ measurements of the aerosol
50 absorption coefficient, aerosol particle number concentration and size distribution of cloud particle
51 residuals and ambient aerosol particles during the ALOUD campaign in May and June 2017.
52 <https://doi.org/10.1594/PANGAEA.900403>.
53
54 Milbrandt, J. A. and Yau, M. K., 2005a. A multi-moment bulk microphysics parametrization. Part I:
55 Analysis of the role of the spectral shape parameter. *J. Atmos. Sci.* 62, 3051–3064.
56 <https://doi.org/10.1175/JAS3534.1>.

1
2 Milbrandt, J. A. and Yau, M. K., 2005b. A multi-moment bulk microphysics parametrization. Part II: A
3 proposed three-moment closure and scheme description. *J. Atmos. Sci.* 62, 3065–3081.
4 <https://doi.org/10.1175/JAS3535.1>.
5
6 Mioche, G., Jourdan, O., 2018. Chapter 6 - Spaceborne Remote Sensing and Airborne In Situ
7 Observations of Arctic Mixed-Phase Clouds, in: Andronache, C. (Ed.), *Mixed-Phase Clouds*. Elsevier,
8 pp. 121–150. <https://doi.org/10.1016/B978-0-12-810549-8.00006-4>
9
10 Mioche, G., Jourdan, O., Ceccaldi, M., Delanoë, J., 2015. Variability of mixed-phase clouds in the Arctic
11 with a focus on the Svalbard region: a study based on spaceborne active remote sensing. *Atmospheric*
12 *Chemistry and Physics* 15, 2445–2461. <https://doi.org/10.5194/acp-15-2445-2015>
13
14 Mioche, G., Jourdan, O., Delanoë, J., Gourbeyre, C., Febvre, G., Dupuy, R., et al., 2017. Vertical
15 distribution of microphysical properties of Arctic springtime low-level mixed-phase clouds over the
16 Greenland and Norwegian seas. *Atmos. Chem. Phys.* 17, 12845–12869. [https://doi.org/10.5194/acp-](https://doi.org/10.5194/acp-17-12845-2017)
17 [17-12845-2017](https://doi.org/10.5194/acp-17-12845-2017).
18
19 Monin, A. S. and Obukhov, A. M., 1954. Basic laws of turbulent mixing in the surface layer of the
20 atmosphere. *Contrib. Geophys. Inst. Acad. Sci. USSR* 151, 163–187.
21
22 Morrison, H., Thompson, G., and Tatarskii, V., 2009. Impact of Cloud Microphysics on the Development
23 of Trailing Stratiform Precipitation in a Simulated Squall Line: Comparison of One and Two-Moment
24 Schemes. *Mon. Wea. Rev.* 137, 991–1007. <https://doi.org/10.1175/2008MWR2556.1>.
25
26 Morrison, H., de Boer, G., Feingold, G., Harrington, J., Shupe, M.D., Sulia, K., 2012. Resilience of
27 persistent Arctic mixed-phase clouds. *Nature Geosci* 5, 11–17. <https://doi.org/10.1038/ngeo1332>.
28
29 Morrison, H., and Milbrandt, J. A. 2015. Parameterization of Cloud Microphysics Based on the Prediction
30 of Bulk Ice Particle Properties. Part I: Scheme Description and Idealized Tests. *J. Atmos. Sci.*, 72, 287–
31 311, <https://doi.org/10.1175/JAS-D-14-0065.1>.
32
33 Moser, M., Voigt, C., Jurkat-Witschas, T., Hahn, V., Mioche, G., Jourdan, O., Dupuy, R., Gourbeyre, C.,
34 Schwarzenboeck, A., Lucke, J., Boose, Y., Mech, M., Borrmann, S., Ehrlich, A., Herber, A., Lüpkes, C.,
35 Wendisch, M., 2023. Microphysical and thermodynamic phase analyses of Arctic low-level clouds
36 measured above the sea ice and the open ocean in spring and summer. *Atmospheric Chemistry and*
37 *Physics* 23, 7257–7280. <https://doi.org/10.5194/acp-23-7257-2023>
38
39 Murray, B.J., O’Sullivan, D., Atkinson, J.D., Webb, M.E., 2012. Ice nucleation by particles immersed in
40 supercooled cloud droplets. *Chem. Soc. Rev.* 41, 6519–6554. <https://doi.org/10.1039/C2CS35200A>
41
42 Nakanishi, M. and Niino, H., 2006. An Improved Mellor-Yamada Level 3 Model: Its Numerical Stability
43 and Application to a Regional Prediction of Advection Fog. *Boundary-Layer Meteorology.* 119, 397–407.
44 <https://doi.org/10.1007/s10546-005-9030-8>.
45
46 Nakanishi, M. and Niino, H., 2009. Development of an improved turbulence closure model for the
47 atmospheric boundary layer. *J. Meteorol. Soc. Japan. Ser. II.* 87, 895–912.
48 <https://doi.org/10.2151/jmsj.87.895>.
49
50 [Dataset] Neuber, R., Schmidt, L. V., Ritter, C., and Mech, M., 2019. Cloud top altitudes observed with
51 airborne lidar during the ACLOUD campaign. <https://doi.org/10.1594/PANGAEA.899962>.
52
53 Nygård, T., Valkonen, T., Vihma, T., 2014. Characteristics of Arctic low-tropospheric humidity inversions
54 based on radio soundings. *Atmos. Chem. Phys.* 14, 1959–1971. [https://doi.org/10.5194/acp-14-1959-](https://doi.org/10.5194/acp-14-1959-2014)
55 [2014](https://doi.org/10.5194/acp-14-1959-2014).
56

1 Ori, D., von Terzi, L., Karrer, M., and Kneifel, S., 2021. SnowScatt 1.0: consistent model of microphysical
2 and scattering properties of rimed and unrimed snowflakes based on the self-similar Rayleigh-Gans
3 approximation. *Geosci. Model Dev.* 14, 1511–1531. <https://doi.org/10.5194/gmd-14-1511-2021>.
4
5 Oue, M., Tatarevic, A., Kollias, P., Wang, D., Yu, K., and Vogelmann, A. M., 2020. The Cloud-resolving
6 model Radar SIMulator (CR-SIM) Version 3.3: description and applications of a virtual observatory.
7 *Geosci. Model Dev.* 13, 1975–1998. <https://doi.org/10.5194/gmd-13-1975-2020>.
8
9 Ovchinnikov, M., Ackerman, A.S., Avramov, A., Cheng, A., Fan, J., Fridlind, A.M., Ghan, S., Harrington,
10 J., Hoose, C., Korolev, A., McFarquhar, G.M., Morrison, H., Paukert, M., Savre, J., Shipway, B.J.,
11 Shupe, M.D., Solomon, A., Sulia, K., 2014. Intercomparison of large-eddy simulations of Arctic mixed-
12 phase clouds: Importance of ice size distribution assumptions. *Journal of Advances in Modeling Earth*
13 *Systems* 6, 223–248. <https://doi.org/10.1002/2013MS000282>
14
15 Pasquier, J. T., Henneberger, J., Ramelli, F., Lauber, A., David, R. O., Wieder, J., Carlsen, T., Gierens,
16 R., Maturilli, M., and Lohmann, U., 2022. Conditions favorable for secondary ice production in Arctic
17 mixed-phase clouds. *Atmos. Chem. Phys.*, 22, 15579–15601, [https://doi.org/10.5194/acp-22-15579-](https://doi.org/10.5194/acp-22-15579-2022)
18 [2022](https://doi.org/10.5194/acp-22-15579-2022).
19
20 Pithan, F., Ackerman, A., Angevine, W.M., Hartung, K., Ickes, L., Kelley, M., Medeiros, B., Sandu, I.,
21 Steeneveld, G.-J., Sterk, H., Svensson, G., Vaillancourt, P.A., Zadra, A., 2016. Select strengths and
22 biases of models in representing the Arctic winter boundary layer over sea ice: the Larcform 1 single
23 column model intercomparison. *J Adv Model Earth Syst* 8, 1345–1357.
24 <https://doi.org/10.1002/2016MS000630>
25
26 Planche, C., Mann, G. W., Carslaw, K. S., Dalvi, M., Marsham, J. H., and Field, P. R., 2017. Spatial and
27 temporal CCN variations in convection-permitting aerosol microphysics simulations in an idealized
28 marine tropical domain. *Atmos. Chem. Phys.* 17, 3371–3384. [https://doi.org/10.5194/acp-17-3371-](https://doi.org/10.5194/acp-17-3371-2017)
29 [2017](https://doi.org/10.5194/acp-17-3371-2017).
30
31 Planche, C., Marsham, J., Field, P., Carslaw, K., Hill, A., Mann, G., and Shipway, B. 2015. Precipitation
32 sensitivity to autoconversion rate in a Numerical Weather Prediction Model. *Q. J. R. Meteorol. Soc.* 141,
33 2032–2044. DOI: 10.1002/qj.2497
34
35 Planche, C., Tridon, F., Banson, S., Thompson, G., Monier, M., Battaglia, A., et al., 2019. On the Realism
36 of the Rain Microphysics Representation of a Squall Line in the WRF Model. Part II: Sensitivity Studies
37 on the Rain Drop Size Distributions. *Mon. Wea. Rev.* 147, 2811–2825. [https://doi.org/10.1175/MWR-D-](https://doi.org/10.1175/MWR-D-18-0019.1)
38 [18-0019.1](https://doi.org/10.1175/MWR-D-18-0019.1).
39
40 Planche, C., Wobrock, W., and Flossmann, A. 2014. The continuous melting process in a cloud scale
41 model using a bin microphysics scheme. *Q. J. R. Meteorol. Soc.* 140, 1986–1996. [https://](https://doi.org/10.1002/qj.2265)
42 doi.org/10.1002/qj.2265
43
44 Planche, C., Wobrock, W., Flossmann, A., Tridon, F., Van Baelen, J., Pointin, Y., and Hagen, M. 2010.
45 The influence of aerosol particle number and hygroscopicity on the evolution of convective cloud
46 systems and their precipitation: A numerical study based on the COPS observations on 12 August 2007.
47 *Atm. Res.* 98, 40–56. <https://doi.org/10.1016/j.atmosres.2010.05.003>.
48
49 Prenni, A.J., Harrington, J.Y., Tjernström, M., DeMott, P.J., Avramov, A., Long, C.N., Kreidenweis, S.M.,
50 Olsson, P.Q., Verlinde, J., 2007. Can Ice-Nucleating Aerosols Affect Arctic Seasonal Climate? *Bulletin*
51 *of the American Meteorological Society* 88, 541–550. <https://doi.org/10.1175/BAMS-88-4-541>
52
53 Ruiz-Donoso, E., Ehrlich, A., Schäfer, M., Jäkel, E., Schemann, V., Crewell, S., et al., 2020. Small-scale
54 structure of thermodynamic phase in Arctic mixed-phase clouds observed by airborne remote sensing
55 during a cold air outbreak and a warm air advection event. *Atmos. Chem. Phys.* 20, 5487–5511.
56 <https://doi.org/10.5194/acp-20-5487-2020>.

1
2 Savre, J., Ekman, A. M. L., Svensson, G., and Tjernström, M., 2014. Large-eddy simulations of an Arctic
3 mixed-phase stratiform cloud observed during ISDAC: sensitivity to moisture aloft, surface fluxes and
4 large-scale forcing. *Quart. J. Roy. Meteorol. Soc.* 141, 1177–1190. <https://doi.org/10.1002/qj.2425>.
5
6 Savre, J., Ekman, A.M.L., 2015a. Large-eddy simulation of three mixed-phase cloud events during
7 ISDAC: Conditions for persistent heterogeneous ice formation. *Journal of Geophysical Research:*
8 *Atmospheres* 120, 7699–7725. <https://doi.org/10.1002/2014JD023006>
9
10 Savre, J., Ekman, A.M.L., Svensson, G., Tjernström, M., 2015b. Large-eddy simulations of an Arctic
11 mixed-phase stratiform cloud observed during ISDAC: sensitivity to moisture aloft, surface fluxes and
12 large-scale forcing. *Quarterly Journal of the Royal Meteorological Society* 141, 1177–1190.
13 <https://doi.org/10.1002/qj.2425>
14
15 Shupe, M.D., Intrieri, J.M., 2004. Cloud Radiative Forcing of the Arctic Surface: The Influence of Cloud
16 Properties, Surface Albedo, and Solar Zenith Angle. *Journal of Climate* 17, 616–628.
17 [https://doi.org/10.1175/1520-0442\(2004\)017<0616:CRFOTA>2.0.CO;2](https://doi.org/10.1175/1520-0442(2004)017<0616:CRFOTA>2.0.CO;2).
18
19 Shupe, M.D., Matrosov, S.Y., Uttal, T., 2006. Arctic Mixed-Phase Cloud Properties Derived from
20 Surface-Based Sensors at SHEBA. *Journal of the Atmospheric Sciences* 63, 697–711.
21 <https://doi.org/10.1175/JAS3659.1>
22
23 Shupe, M.D., Walden, V.P., Eloranta, E., Uttal, T., Campbell, J.R., Starkweather, S.M., Shiobara, M.,
24 2011. Clouds at Arctic Atmospheric Observatories. Part I: Occurrence and Macrophysical Properties.
25 *Journal of Applied Meteorology and Climatology* 50, 626–644. <https://doi.org/10.1175/2010JAMC2467.1>
26
27 Skamarock, W. C., Klemp, J. B., Dudhia, J., Gill, D. O., Baker, D. M., Duda, M. G., et al., 2008. A
28 Description of the Advanced Research WRF Version 3 (NCAR/TN-475+STR Technical Note, 125 pp.).
29
30 Solomon, A., de Boer, G., Creamean, J.M., McComiskey, A., Shupe, M.D., Maahn, M., Cox, C., 2018.
31 The relative impact of cloud condensation nuclei and ice nucleating particle concentrations on phase
32 partitioning in Arctic mixed-phase stratocumulus clouds. *Atmospheric Chemistry and Physics* 18,
33 17047–17059. <https://doi.org/10.5194/acp-18-17047-2018>
34
35 Solomon, A., Shupe, M.D., Persson, P.O.G., Morrison, H., 2011. Moisture and dynamical interactions
36 maintaining decoupled Arctic mixed-phase stratocumulus in the presence of a humidity inversion.
37 *Atmos. Chem. Phys.* 11, 10127–10148. <https://doi.org/10.5194/acp-11-10127-2011>
38
39 Solomon, A., Feingold, G., Shupe, M.D., 2015. The role of ice nuclei recycling in the maintenance of
40 cloud ice in Arctic mixed-phase stratocumulus. *Atmospheric Chemistry and Physics* 15, 10631–10643.
41 <https://doi.org/10.5194/acp-15-10631-2015>
42
43 Sotiropoulou, G., Tjernström, M., Savre, J., Ekman, A.M.L., Hartung, K., Sedlar, J., 2018. Large-eddy
44 simulation of a warm-air advection episode in the summer Arctic. *Quarterly Journal of the Royal*
45 *Meteorological Society* 144, 2449–2462. <https://doi.org/10.1002/qj.3316>
46
47 Sorteberg, A. and Walsh, J. E., 2008. Seasonal cyclone variability at 70°N and its impact on moisture
48 transport into the Arctic. *Tellus A.* 60, 570–586. <https://doi.org/10.1111/j.1600-0870.2007.00314.x>.
49
50 Stachlewska, I. S., Neuber, R., Lampert, A., Ritter, C., and Wehrle, G., 2010. AMALi-the Airborne Mobile
51 Aerosol Lidar for Arctic research. *Atmos. Chem. Phys.* 10, 2947–2963. <https://doi.org/10.5194/acp-10-2947-2010>.
52
53
54 Stapf, J., Ehrlich, A., Jäkel, E., Lüpkes, C., and Wendisch, M., 2020. Reassessment of shortwave
55 surface cloud radiative forcing in the Arctic: consideration of surface-albedo-cloud interactions. *Atmos.*
56 *Chem. Phys.* 20, 9895–9914. <https://doi.org/10.5194/acp-20-9895-2020>.

1
2 [Dataset] Stapf, J., Ehrlich, A., Jäkel, E., and Wendisch, M., 2019a. Aircraft measurements of broadband
3 irradiance during the ACLOUD campaign in 2017. <https://doi.org/10.1594/PANGAEA.900442>.
4
5 [Dataset] Stapf, J., Ehrlich, A., Jäkel, E., and Wendisch, M., 2019b. Cloud radiative forcing, LWP and
6 cloud-free albedo derived from airborne broadband irradiance observations during the ACLOUD
7 campaign. <https://doi.org/10.1594/PANGAEA.909289>.
8
9 Stevens, R. G., Loewe, K., Dearden, C., Dimitrellos, A., Possner, A., Eirund, G. K., Raatikainen, T., Hill,
10 A. A., Shipway, B. J., Wilkinson, J., Romakkaniemi, S., Tonttila, J., Laaksonen, A., Korhonen, H.,
11 Connolly, P., Lohmann, U., Hoose, C., Ekman, A. M. L., Carslaw, K. S., and Field, P. R., 2018. A model
12 intercomparison of CCN-limited tenuous clouds in the high Arctic. *Atmos. Chem. Phys.*, 18, 11041–
13 11071, <https://doi.org/10.5194/acp-18-11041-2018>.
14
15 Tan, I., Storelvmo, T., 2019. Evidence of Strong Contributions From Mixed-Phase Clouds to Arctic
16 Climate Change. *Geophys. Res. Lett.* 46, 2894–2902. <https://doi.org/10.1029/2018GL081871>
17
18 Thompson, G., and Eidhammer, T. 2014. A Study of Aerosol Impacts on Clouds and Precipitation
19 Development in a Large Winter Cyclone. *J. Atmos. Sci.*, 71, 3636–3658, [https://doi.org/10.1175/JAS-D-](https://doi.org/10.1175/JAS-D-13-0305.1)
20 [13-0305.1](https://doi.org/10.1175/JAS-D-13-0305.1).
21
22 Tjernström, M., Leck, C., Birch, C. E., Bottenheim, J. W., Brooks, B. J., Brooks, I. M., et al., 2014. The
23 Arctic Summer Cloud Ocean Study (ASCOS): overview and experimental design. *Atmos. Chem. Phys.*
24 14, 2823–2869. <https://doi.org/10.5194/acp-14-2823-2014>.
25
26 Tjernström, M. and Graverson, R., 2009. The vertical structure of the lower Arctic troposphere analyzed
27 from observations and the ERA-40 reanalysis. *Q. J. R. Meteorol. Soc.* 135, 431–443.
28 <https://doi.org/10.1002/qj.380>.
29
30 Tjernström, M., Sedlar, J., Shupe, M.D., 2008. How Well Do Regional Climate Models Reproduce
31 Radiation and Clouds in the Arctic? An Evaluation of ARCMIP Simulations. *Journal of Applied*
32 *Meteorology and Climatology* 47, 2405–2422. <https://doi.org/10.1175/2008JAMC1845.1>
33
34 Tridon, F., Battaglia, A., Chase, R. J., Turk, F. J., Leinonen, J., Kneifel, S., et al., 2019a. The
35 microphysics of stratiform precipitation during OLYMPEX: Compatibility between triple-frequency radar
36 and airborne in situ observations. *J. Geophys. Res. - Atmos.* 124, 8764–8792.
37 <https://doi.org/10.1029/2018JD029858>.
38
39 Tridon, F., Planche, C., Mroz, K., Banson, S., Battaglia, A., Van Baelen, J., et al., 2019b. On the Realism
40 of the Rain Microphysics Representation of a Squall Line in the WRF Model. Part I: Evaluation with
41 Multifrequency Cloud Radar Doppler Spectra Observations. *Mon. Wea. Rev.* 147, 2787–2810.
42 <https://doi.org/10.1175/MWR-D-18-0018.1>.
43
44 Twohy, C., Strapp, J., and Wendisch, M., 2003. Performance of a Counterflow Virtual Impactor in the
45 NASA Icing Research Tunnel. *J. Atmos. Ocean. Technol.* 20, 781–790. [https://doi.org/10.1175/1520-](https://doi.org/10.1175/1520-0426(2003)020(0781:POACVI)2.0.CO)
46 [0426\(2003\)020\(0781:POACVI\)2.0.CO](https://doi.org/10.1175/1520-0426(2003)020(0781:POACVI)2.0.CO).
47
48 Waitz, F., Schnaiter, M., Leisner, T., Järvinen, E., 2022. In situ observation of riming in mixed-phase
49 clouds using the PHIPS probe. *Atmospheric Chemistry and Physics* 22, 7087–7103.
50 <https://doi.org/10.5194/acp-22-7087-2022>
51
52 Wendisch, M., and J.-L. Brenguier (Eds.), 2013: Airborne Measurements for Environmental Research:
53 Methods and Instruments. *Wiley-VCH Verlag GmbH & Co. KGaA, Weinheim, Germany*.
54 ISBN: 978-3-527-40996-9. 655 pp., doi:10.1002/9783527653218

55

1 Wendisch, M., Brückner, M., Burrows, J. P., Crewell, S., Dethloff, K., Ebell, K., et al., 2017. Arctic
2 Amplification: Climate Relevant Atmospheric and Surface Processes, and Feedback Mechanisms
3 (AC)³. *Eos, Trans. Amer. Geophys. Union.* 98. <https://doi.org/10.1029/2017EO064803>.
4
5 Wendisch, M., Macke, A., Ehrlich, A., Lüpkes, C., Mech, M., Chechin, D., et al., 2019. The Arctic Cloud
6 Puzzle: Using ALOUD/PASCAL Multiplatform Observations to Unravel the Role of Clouds and Aerosol
7 Particles in Arctic Amplification. *Bull. Amer. Meteorol. Soc.* 100, 841–871.
8 <https://doi.org/10.1175/BAMS-D-18-0072.1>.
9
10 Wendisch, M., Stapf, J., Becker, S., Ehrlich, A., Jäkel, E., Klingebiel, M., Lüpkes, C., Schäfer, M., and
11 Shupe, M. D., 2023a Effects of variable ice-ocean surface properties and air mass transformation on
12 the Arctic radiative energy budget, *Atmos. Chem. Phys.* 23, 9647–9667, [https://doi.org/10.5194/acp-23-](https://doi.org/10.5194/acp-23-9647-2023)
13 [9647-2023](https://doi.org/10.5194/acp-23-9647-2023)
14 Wendisch, M., Brückner, M., Crewell, S., Ehrlich, A., Notholt, J., Lüpkes, C., et al., 2023b. Atmospheric
15 and Surface Processes, and Feedback Mechanisms Determining Arctic Amplification: A Review of First
16 Results and Prospects of the (AC)³ Project. *Bull. Amer. Meteorol. Soc.* 104, E208–E242.
17 <https://doi.org/10.1175/BAMS-D-21-0218.1>.
18
19 Wesche, C., Steinhage, D., and Nixdorf, U., 2016. Polar aircraft Polar 5 and Polar 6 operated by the
20 Alfred Wegener Institute. *J. Large Scale Res. Facilities.* 2. <https://doi.org/10.17815/jlsrf-2-153>.
21
22 Wex, H., Huang, L., Zhang, W., Hung, H., Traversi, R., Becagli, S., Sheesley, R.J., Moffett, C.E., Barrett,
23 T.E., Bossi, R., Skov, H., Hünerbein, A., Lubitz, J., Löffler, M., Linke, O., Hartmann, M., Herenz, P.,
24 Stratmann, F., 2019. Annual variability of ice-nucleating particle concentrations at different Arctic
25 locations. *Atmospheric Chemistry and Physics* 19, 5293–5311. [https://doi.org/10.5194/acp-19-5293-](https://doi.org/10.5194/acp-19-5293-2019)
26 [2019](https://doi.org/10.5194/acp-19-5293-2019)
27
28 Woods, C., Caballero, R., and Svensson, G., 2013. Large-scale circulation associated with moisture
29 intrusions into the Arctic during winter. *Geophys. Res. Lett.* 40, 4717–4721.
30 <https://doi.org/10.1002/grl.50912>.
31
32 Xue, J., Xiao, Z., Bromwich, D. H., and Bai, L., 2022. Polar WRF V4.1.1 simulation and evaluation for
33 the Antarctic and Southern Ocean. *Front. Earth Sci.* 16, 1005–1024. [https://doi.org/10.1007/s11707-](https://doi.org/10.1007/s11707-022-0971-8)
34 [022-0971-8](https://doi.org/10.1007/s11707-022-0971-8).
35
36 Young, G., Jones, H. M., Choularton, T. W., Crosier, J., Bower, K. N., Gallagher, M. W., et al., 2016.
37 Observed microphysical changes in Arctic mixed-phase clouds when transitioning from sea ice to open
38 ocean. *Atmos. Chem. Phys.* 16, 13945–13967. <https://doi.org/10.5194/acp-16-13945-2016>.
39
40 Young, G., Connolly, P.J., Jones, H.M., Choularton, T.W., 2017. Microphysical sensitivity of coupled
41 springtime Arctic stratocumulus to modelled primary ice over the ice pack, marginal ice, and ocean.
42 *Atmospheric Chemistry and Physics* 17, 4209–4227. <https://doi.org/10.5194/acp-17-4209-2017>.
43
44 Young, G., Connolly, P. J., Dearden, C., and Choularton, T. W., 2018. Relating large-scale subsidence
45 to convection development in Arctic mixed-phase marine stratocumulus, *Atmos. Chem. Phys.*, 18,
46 1475–1494, <https://doi.org/10.5194/acp-18-1475-2018>.
47
48 Yu, L., Yang, Q., Zhou, M., Zeng, X., Lenschow, D. H., Wang, X., et al., 2019. The Intraseasonal and
49 Interannual Variability of Arctic Temperature and Specific Humidity Inversions. *Atmosphere.* 10(4).
50 <https://doi.org/10.3390/atmos10040214>.
51
52 [Dataset] Zanatta, M., and Herber, A., 2019. Aircraft measurements of aerosol size distribution in the
53 Arctic during the ALOUD campaign 2017. <https://doi.org/10.1594/PANGAEA.900341>.
54

1 Zanatta, M., Mertes, S., Jourdan, O., Dupuy, R., Järvinen, E., Schnaiter, M., Eppers, O., Schneider, J.,
2 Jurányi, Z., and Herber, A., 2023. Airborne investigation of black carbon interaction with low-level,
3 persistent, mixed-phase clouds in the Arctic summer, *Atmos. Chem. Phys.*, 23, 7955–7973,
4 <https://doi.org/10.5194/acp-23-7955-2023>.

5
6 Zhao, X., Liu, X., 2022. Primary and secondary ice production: interactions and their relative importance.
7 *Atmospheric Chemistry and Physics* 22, 2585–2600. <https://doi.org/10.5194/acp-22-2585-2022>

8

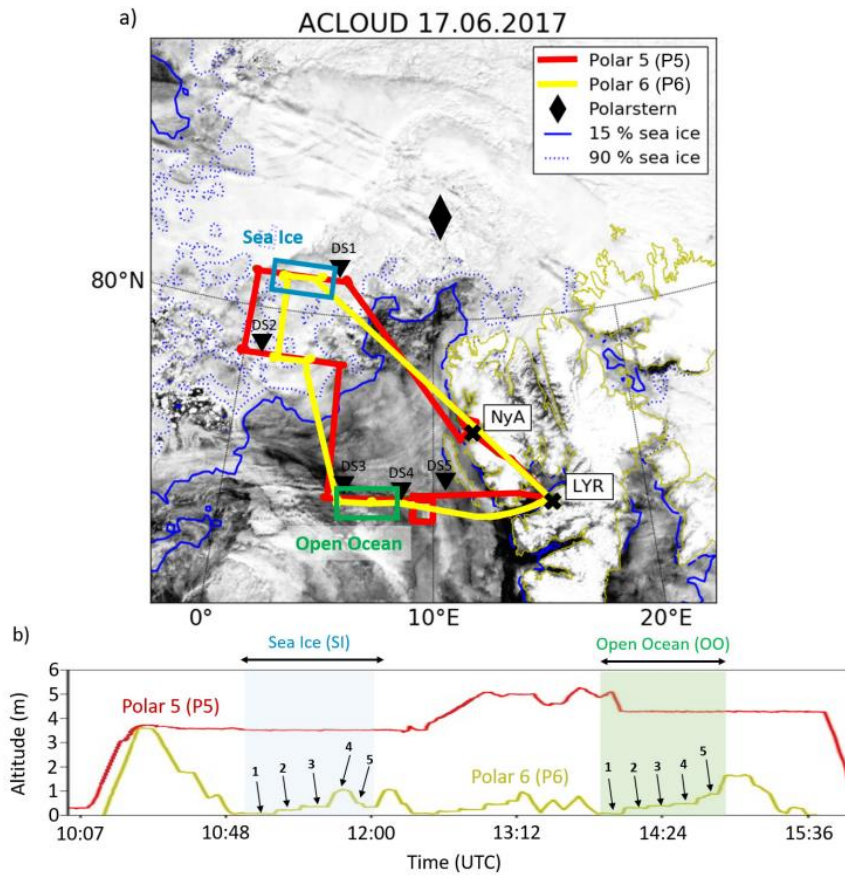
ACCEPTED VERSION FOR PUBLICATION

1 **Figures**

2

3

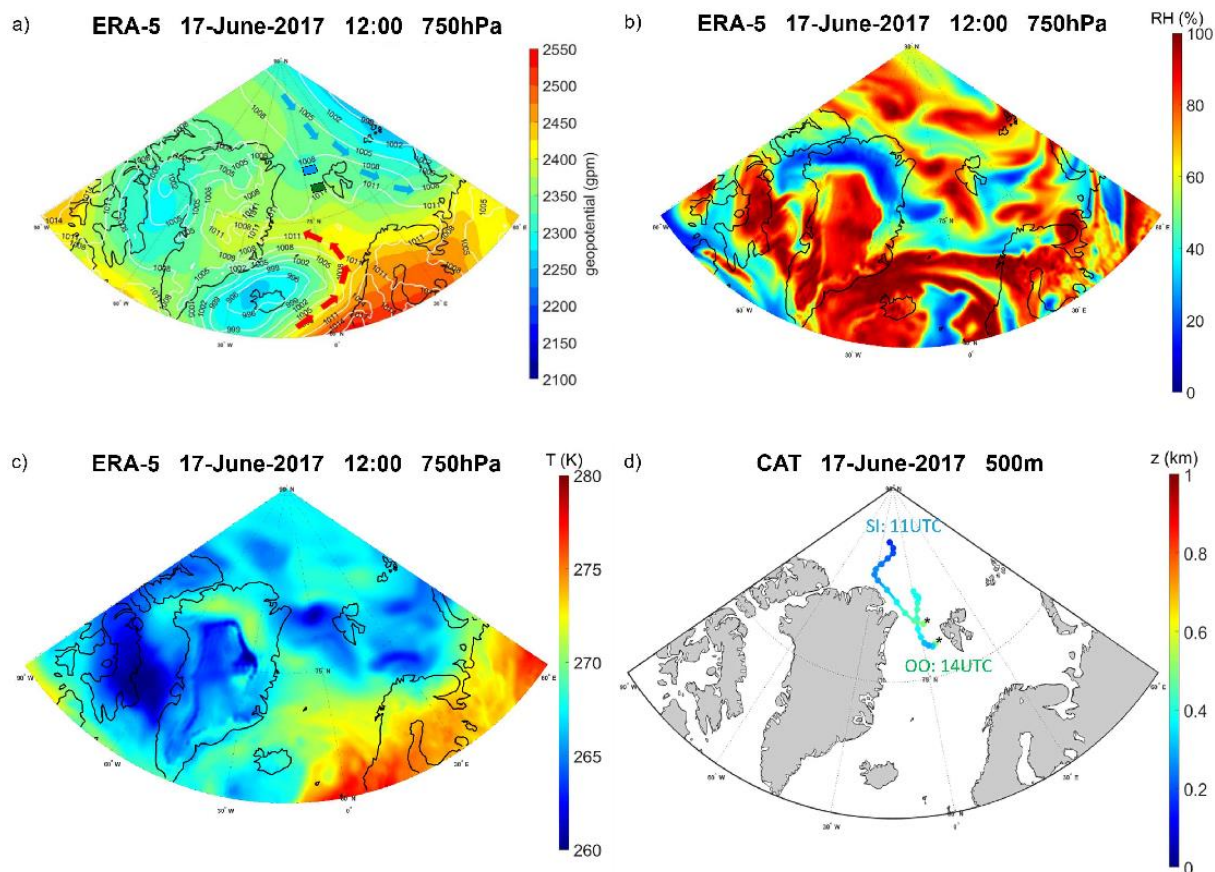
4



5

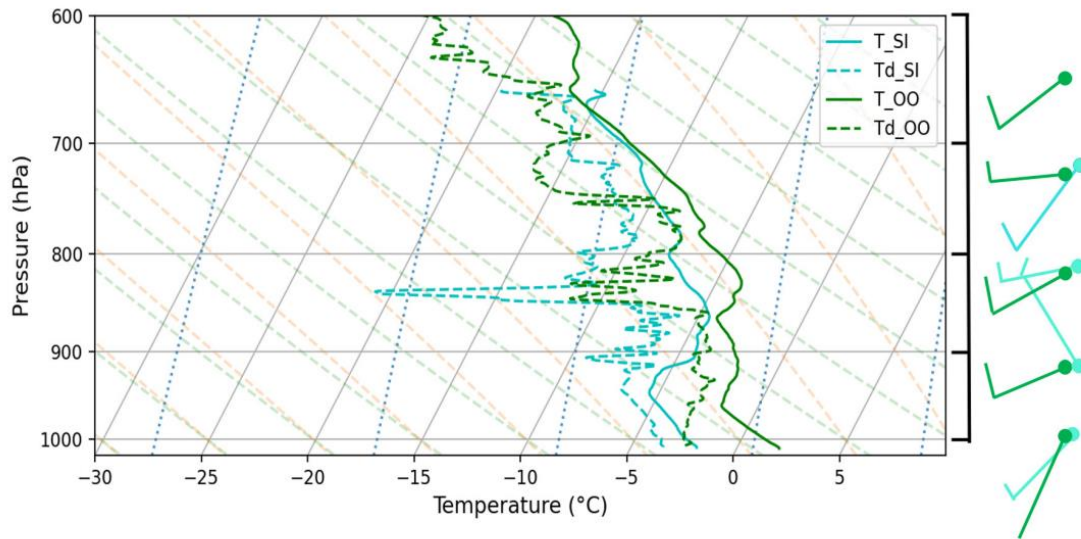
6 **Figure 1.** Flight paths (a) and altitudes (b) for both the Polar 5 (P5, in red)
7 done on 17 June 2017 (*i.e.*, the ACLOUD flight 19). Note that Polar 5 performed three horizontal paths at several
8 constant altitudes. The solid and dotted blue lines indicate the 15% and the 90% sea ice concentration (derived
9 from the AMSR2 measurements; Ludwig et al. (2019)). The white shading represents the cloud cover (visible image
10 from MODIS). Locations where the dropsondes (DS) were released are marked by black triangles. Blue and green
11 rectangles on both panels present the domain analyses for, respectively, the sea ice (SI) and the open ocean (OO)
12 case studies. The small numbers on panel b) indicate the legs (*i.e.*, periods when the aircraft flew at constant
13 altitude) performed by the P6 aircraft. The distance between the SI and OO domains is approximately 245 km.

14



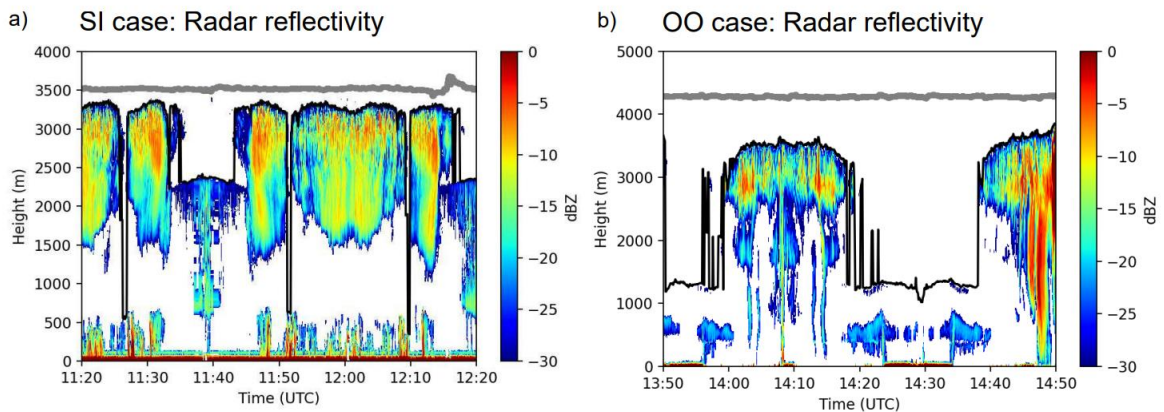
1
 2 **Figure 2.** Synoptic maps of the ERA-5 reanalyse product provided by ECMWF on 17 June 2017 at 12:00 UTC for
 3 (a) the sea level pressure (in hPa; white contours) and the 750 hPa geopotential heights (in meters; colour scale),
 4 (b) the relative humidity (RH) (in %), and (c) the air temperature T (in K). Blue and red arrows on panel (a) represent
 5 the two air masses towards the Svalbard archipelago while the blue and red rectangles present the domain analyses
 6 for, respectively, the sea ice (SI) and the open ocean (OO) case studies (see also Figure 1a). Panel (d) illustrates
 7 the 72 hours mean mass back-trajectories calculated from the positions represented by the black stars. These start
 8 points correspond to the P6 aircraft position in longitude and in latitude at 11:00 UTC and 14:00 UTC respectively,
 9 and at an altitude of $\approx 500 \pm 200$ m (corresponding to the SI and the OO cases).

10



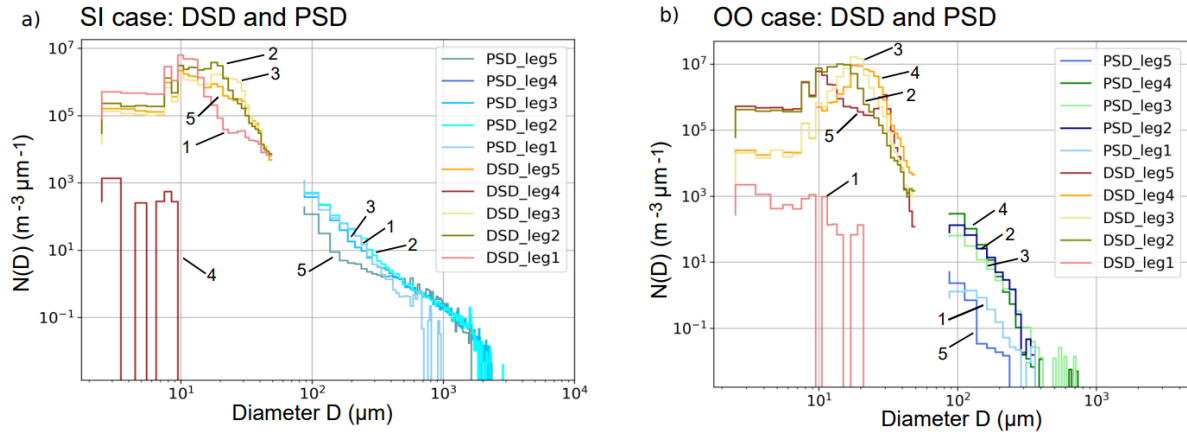
1
 2 **Figure 3.** Skew-T Log-P diagram with the vertical profiles of the air temperature T (solid lines) and the dew point
 3 temperature T_d (dashed lines) measured from the dropsondes DS1 and DS4. These dropsondes are released at
 4 11:20 UTC (DS1) over sea ice surface (SI: in light blue) and at 14:25 UTC (DS4) over open ocean surface (OO: in
 5 green). The positions of DS1 and DS4 are represented in Figure 1a. The bars show the vertical properties of the
 6 horizontal wind speed and direction for both situations.

7



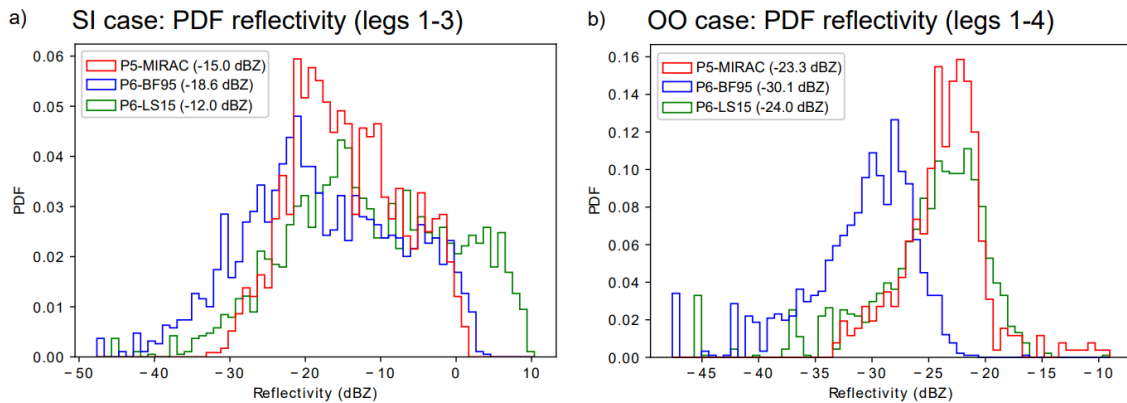
8
 9 **Figure 4.** Temporal evolution of the profile of the radar reflectivity obtained with the 94 GHz MiRAC cloud radar
 10 system deployed on-board the Polar 5 (P5) aircraft for (a) the SI case and (b) the OO case. The grey thick solid
 11 lines represent the P5 flight altitude. The black thin solid lines describe the altitude of the cloud top determined by
 12 the AMALi lidar system. Note that the Polar 5 aircraft turned back several times over the SI (at 11:40 UTC and
 13 12:00 UTC) and OO (at 14:10 UTC and 14:30 UTC) domains.

14



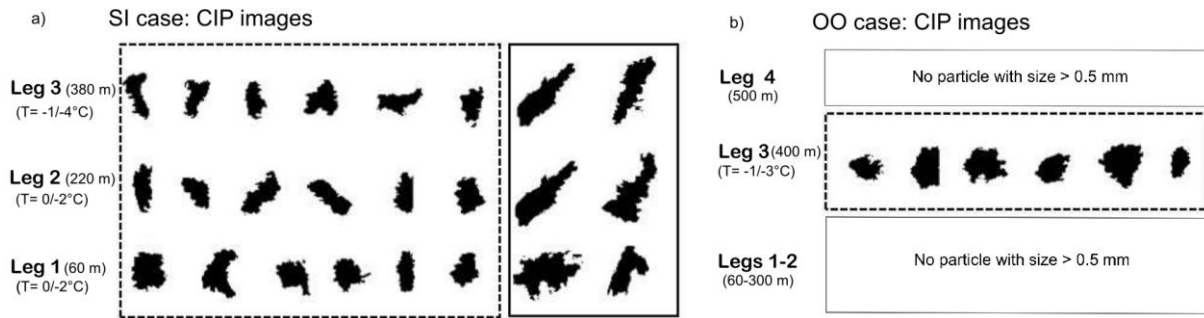
1
2
3
4
5
6
7

Figure 5. Median (calculated with ≈ 350 individual spectra for each leg) droplet size distributions (DSDs) and hydrometeor size distributions with size larger than $75 \mu\text{m}$ (PSDs) calculated for the different legs of the Polar 6 (P6) aircraft (described in Figure 1b) for (a) the SI case (*i.e.*, leg 1: 60 m, leg 2: 220 m, leg 3: 380 m, leg 5: 550 m, and leg 4: 1000 m) and (b) the OO case (*i.e.*, leg 1: 60 m, leg 2: 300 m, leg 3: 400 m, leg 4: 500 m, and leg 5: 900 m).

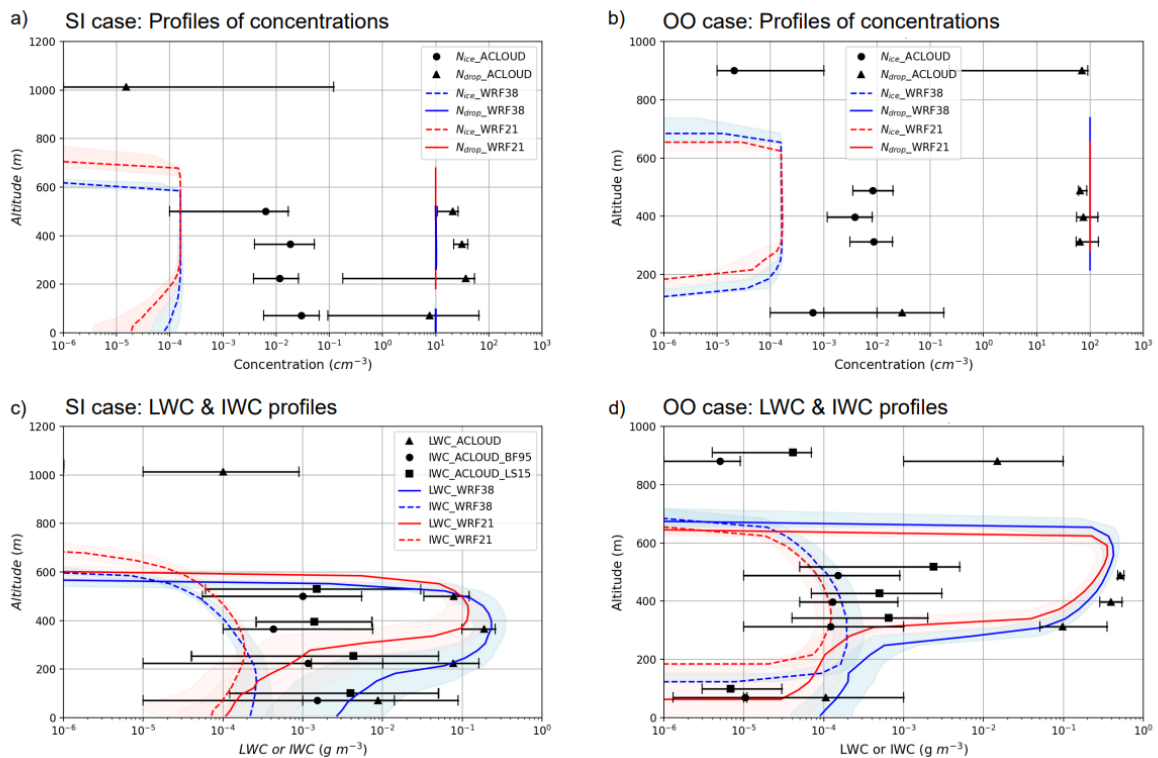


8
9
10
11
12
13
14
15
16

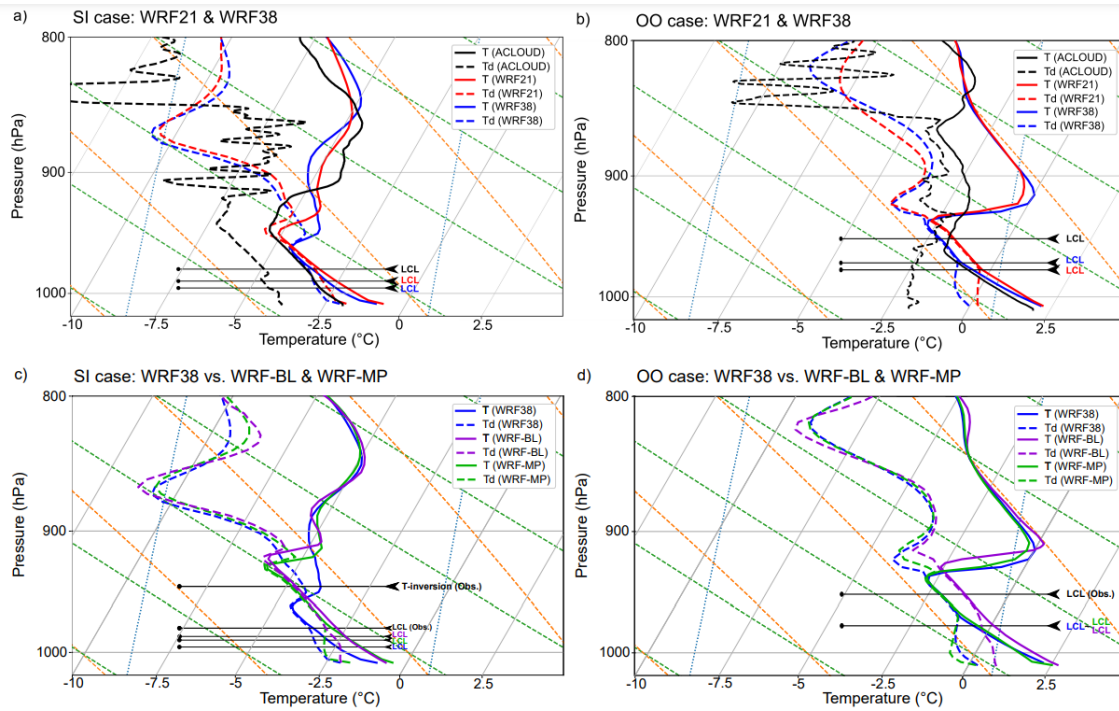
Figure 6. Probability density function (PDF) of the reflectivities measured by the MIRAC cloud radar (deployed on-board the P5) and calculated from *in situ* measurements (deployed on-board the P6) for (a) the SI case and (b) the OO case. The SSRGA associated with two different mass-diameter relations: Brown and Francis (1995) (BF95) or Leinonen and Szyrmer (2015) (LS15), to consider different hypothesis regarding the degree of riming of the ice aggregates, is applied to the *in situ* PSD data to compute the radar reflectivity. Values in the legend indicate the median of the respective parameters.



1
2 **Figure 7.** Examples of CIP images illustrating the presence of slightly rimed aggregates in the different legs. For
3 the OO case, only images for leg 3 are represented due to the small occurrence of ice crystals with sizes larger
4 than 500 μm (see Figure 5b) which is the minimum size for a reasonable analysis of the CIP images. The images
5 enclosed in the dashed and solid black rectangles correspond to aggregates in size ranges 0.5-1 mm and >1 mm,
6 respectively. Temperature ranges (in $^{\circ}\text{C}$) for each leg are also indicated.



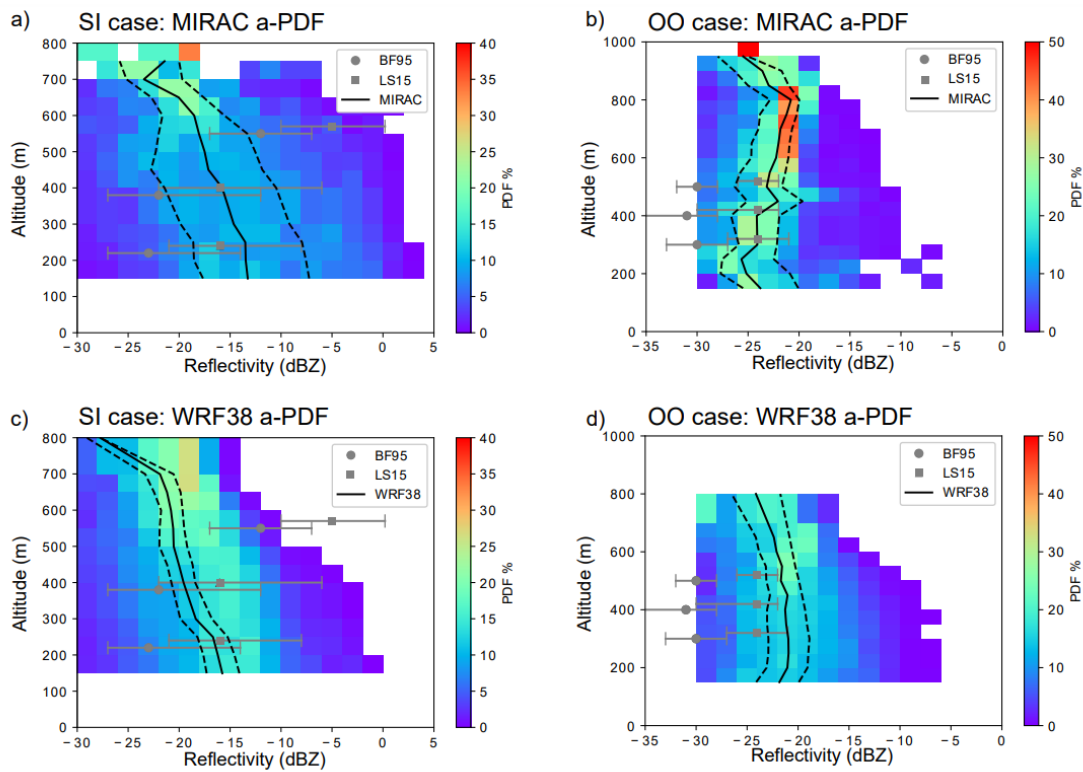
8
9 **Figure 8.** Median vertical profiles of the droplet (N_{drop}) and ice particle (N_{ice}) concentrations (a-b), and of the liquid
10 (LWC) and ice (IWC) water contents (c-d) for the SI case (a,c) and the OO case (b,d) obtained from *in situ* ACloud
11 observations (black circles and squares). For these observations, the IWC are calculated using either the BF95
12 (circles) or the LS15 (squares) mass-diameter relationship. Note that all results obtained using LS15 are plotted
13 with a vertical shift (+30 m) to make the figure easier to read. Symbols correspond to the median values obtained
14 for the different legs and the intervals indicate the first (Q1) and the third (Q3) quartiles. Median profiles (solid lines)
15 and Q1-Q3 spread (coloured shadings) obtained for WRF21 (red) and WRF38 (blue) simulations are also
16 represented. Note that the y-axes are different for both cases.



1

2 **Figure 9.** Mean vertical profiles of the air temperature T (solid lines) and the dew point temperature T_d (dashed
 3 lines) obtained in WRF38 (blue), in WRF21 (red) and from observations (black) for (a) the SI case and (b) the OO
 4 case. Results from the WRF sensitivity studies, WRF-BL (purple) and WRF-MP (green), presented in Section 3.3
 5 for (c) the SI case and (d) the OO case are also illustrated.

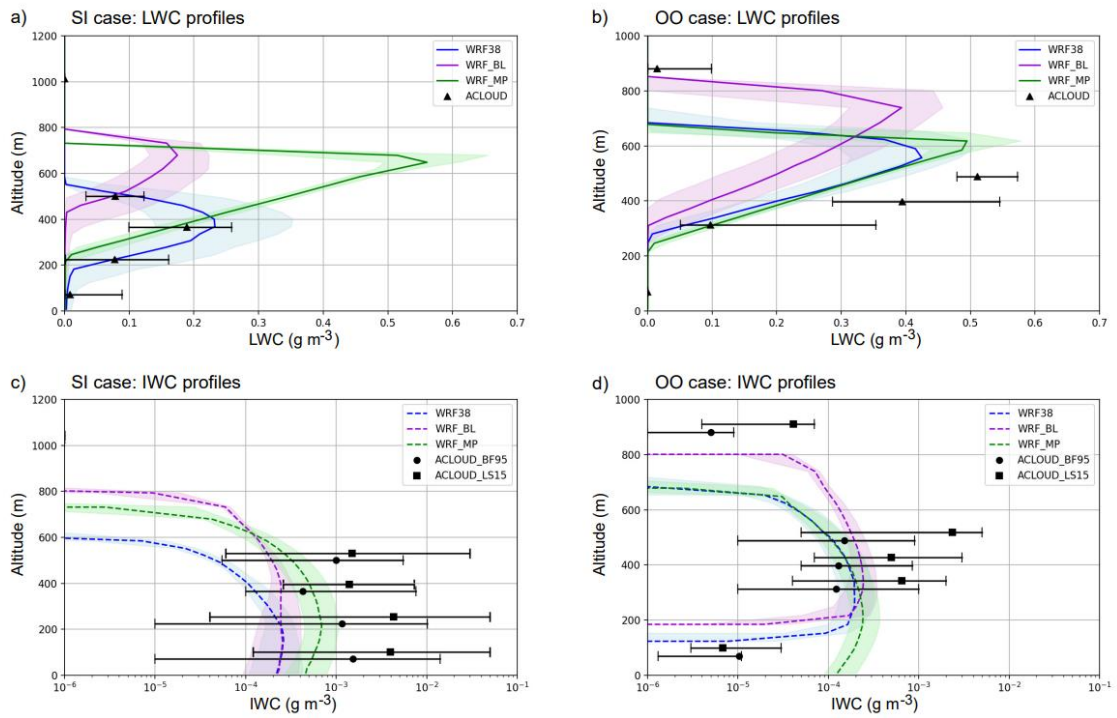
6



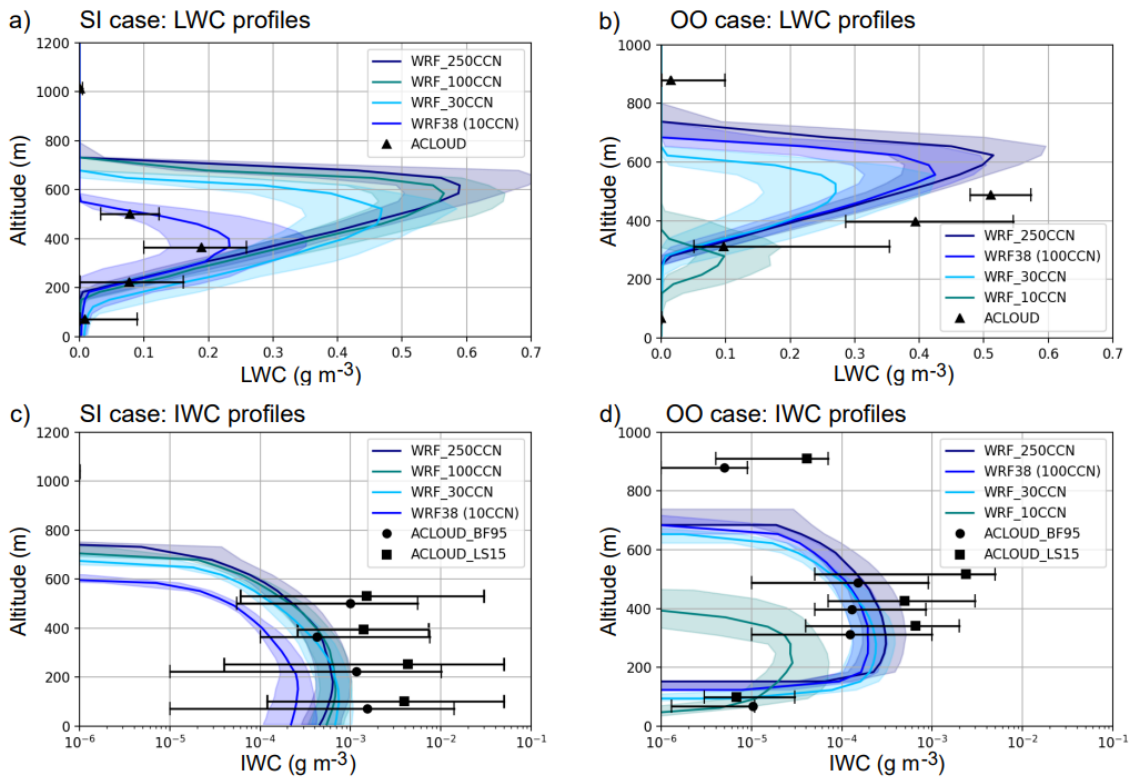
1

2 **Figure 10.** Altitude-dependent probability density function (a-PDFs) of the reflectivities, resolved in bins of 2 dBZ,
 3 from the MiRAC radar system (a-b) and obtained applying the CR-SIM module to the WRF38 simulations (c-d) for
 4 the SI case (a,c) and for OO case (b,d). The a-PDFs are obtained by calculating the PDF for each retrieved level.
 5 Solid black lines represent the median whereas dashed black lines represent the first (Q1) and the third (Q3)
 6 quartiles. Median (grey symbols) and Q1-Q3 spread of the PDF of the reflectivities calculated from *in situ*
 7 measurements using BF95 (circles) or LS15 (squares) are also illustrated. Note that all the results obtained using
 8 LS15 are plotted with a vertical shift (+30 m) to make the figure easier to read.

9

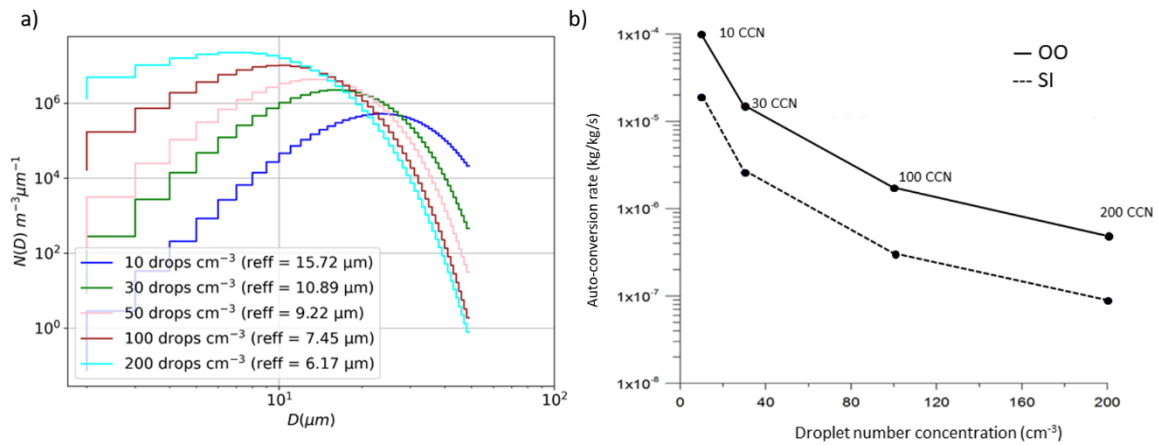


1
 2 **Figure 11.** Median (solid or dashed lines) vertical profiles of the LWC (a-b) and IWC (c-d) for the SI case (a,c) and
 3 the OO case (b,d) simulated in WRF38 (blue), WRF-BL (purple), and WRF-MP (green) experiments. Coloured
 4 shadings represent the Q1-Q3 spread. Observations are indicated by black symbols (compare Figure 8).



5
 6 **Figure 12.** As in Figure 11, but for the different WRF-[n]CCN experiments where [n] = 10 cm⁻³, 30 cm⁻³, 100 cm⁻³,
 7 and 250 cm⁻³. Note that in the WRF38 baseline experiments described in Section 3.2, [n] = 10 cm⁻³ for the SI case
 8 and [n] = 100 cm⁻³ for the OO case.

1



2

3 **Figure 13.** Impacts of the initial droplet number concentration on (a) the drop size distribution (DSD) and the
 4 effective radius, and then on (b) the auto-conversion rate using the MORR microphysics scheme. Panels (a) is
 5 obtained for a given LWC of 0.2 g m^{-3} (typical value encountered in our Sea Ice case). Panel (b) are obtained
 6 considering a LWC equal to 0.2 g m^{-3} for the SI case and 0.4 g m^{-3} for the OO case.

7

ACCEPTED VERSION FOR PUBLICATION